Geophysical Journal International

Geophys. J. Int. (2011) doi: 10.1111/j.1365-246X.2011.05179.x

Lower crustal relaxation beneath the Tibetan Plateau and Qaidam Basin following the 2001 Kokoxili earthquake

Isabelle Ryder[1], Roland Bürgmann[2] and Fred Pollitz[3]

[1] *School of Environmental Sciences, University of Liverpool, UK. E-mail: i.ryder@liv.ac.uk*
[2] *Berkeley Seismological Laboratory, University of California, Berkeley.*
[3] *United States Geological Survey, Menlo Park, CA, USA.*

Accepted 2011 August 1. Received 2011 July 9; in original form 2010 December 23.

SUMMARY

In 2001 November a magnitude 7.8 earthquake ruptured a 400 km long portion of the Kunlun fault, northeastern Tibet. In this study, we analyse over five years of post-seismic geodetic data and interpret the observed surface deformation in terms of stress relaxation in the thick Tibetan lower crust. We model GPS time-series (first year) and InSAR line of sight measurements (years two to five) and infer that the most likely mechanism of post-seismic stress relaxation is time-dependent distributed creep of viscoelastic material in the lower crust. Since a single relaxation time is not sufficient to model the observed deformation, viscous flow is modelled by a lower crustal Burgers rheology, which has two material relaxation times. The optimum model has a transient viscosity 9×10^{17} Pa s, steady-state viscosity 1×10^{19} Pa s and a ratio of long term to Maxwell shear modulus of 2:3. This model gives a good fit to GPS stations south of the Kunlun Fault, while displacements at stations north of the fault are over-predicted. We attribute this asymmetry in the GPS residual to lateral heterogeneity in rheological structure across the southern margin of the Qaidam Basin, with thinner crust/higher viscosities beneath the basin than beneath the Tibetan Plateau. Deep afterslip localized in a shear zone beneath the fault rupture gives a reasonable match to the observed InSAR data, but the slip model does not fit the earlier GPS data well. We conclude that while some localized afterslip likely occurred during the early post-seismic phase, the bulk of the observed deformation signal is due to viscous flow in the lower crust. To investigate regional variability in rheological structure, we also analyse post-seismic displacements following the 1997 Manyi earthquake that occurred 250 km west of the Kokoxili rupture. We find that viscoelastic properties are the same as for the Kokoxili area except for the transient viscosity, which is 5×10^{17} Pa s. The viscosities estimated for the Manyi and Kokoxili areas are consistent with constraints obtained from other earthquakes in the northwest and south central parts of the Tibetan Plateau.

Key words: Satellite geodesy; Seismic cycle; Radar interferometry; Transient deformation; Continental neotectonics; Crustal structure.

1 INTRODUCTION

1.1 Background

The 1500 km-long east–west striking Kunlun fault system in northeastern Tibet (Fig. 1) regularly experiences large earthquakes. Left-lateral strike-slip motion on this fault accommodates eastward motion of the Qiangtang and Songpan-Ganzi terranes on the southern side, relative to the Qaidam Basin on the northern side. Slip rates on the western Kunlun fault have been estimated for the last millennium from dating of offset geomorphic markers (Van der Woerd *et al*. 1998; Woerd *et al*. 2002; Haibing *et al*. 2005) and fall within the small range of ∼10–12 mm yr^{-1}. In the last century, five left-lateral strike-slip earthquakes with magnitude >7 occurred on the Kunlun fault or associated faults at its western end (Xiong *et al*. 2010). The 1937 M_s 7.5 Huashi Canyon earthquake, the 1963 M_s 7.1 Dulan earthquake and the 2001 M_w 7.9 Kokoxili earthquake all occurred on the main Kunlun fault, with increasingly westerly epicentres. The 1973 M_w 7.4 and 1997 M_w 7.6 Manyi earthquakes occurred on a western splay of the main Kunlun fault, rupturing nearby parts of the splay system. The quick succession and close proximity of the 1997 Manyi and 2001 Kokoxili earthquakes provide an unprecedented opportunity to investigate the rheological structure of the crust in this part of Tibet.

In recent decades there has been much interest concerning the rheological nature of the lithosphere beneath the Tibetan Plateau.

© 2011 The Authors
Geophysical Journal International © 2011 RAS

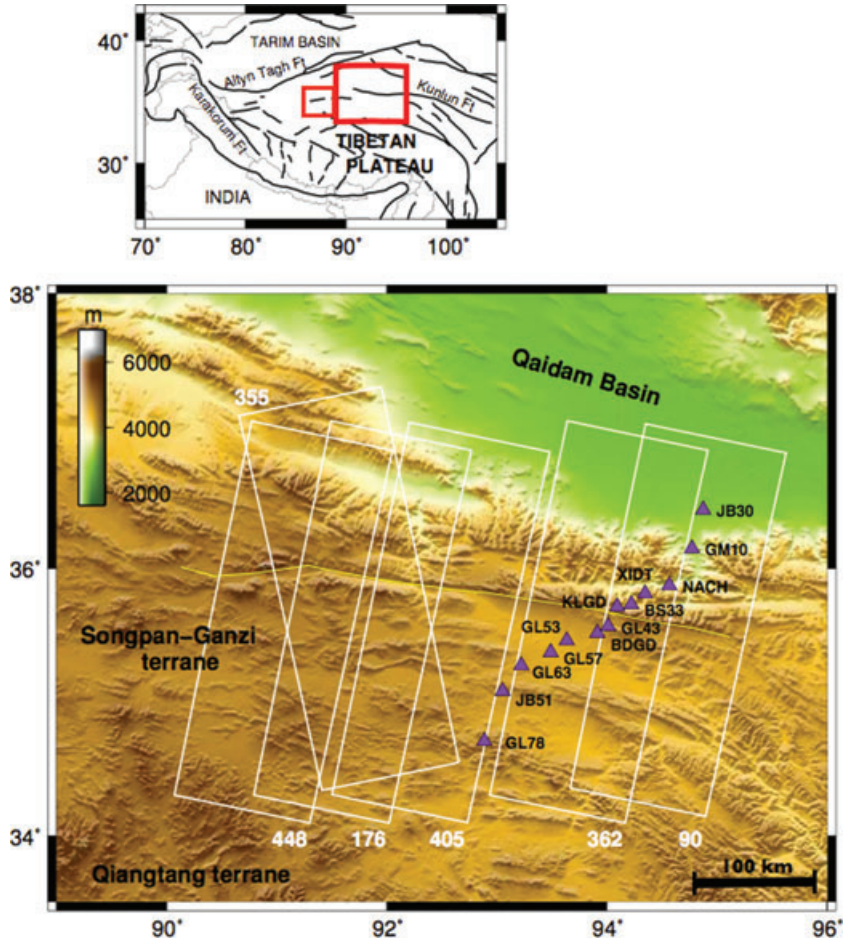

Figure 1. Inset map shows location of study area on the Tibetan Plateau. Large red box outlines area of Kokoxili study and small red box outlines Manyi area. Main image shows topography of the western Kunlun fault area, with shaded relief SRTM digital elevation model. Envisat SAR tracks are marked by white boxes; numbers above/below boxes are track numbers. Purple triangles are GPS sites. Yellow line marks position of fault trace.

In particular, the issue of lower crustal flow has been central to the debate about how the plateau formed and how it is deforming today. The crust across the Tibetan Plateau is much thicker than typical continental crust as a result of the collision between the Indian and Eurasian Plates. The crust thins from about 80 km in the southern plateau to about 55 km in the northern Songpan-Ganzi terrane, immediately south of the Kunlun Fault (e.g. Zhu & Helmberger 1998, Vergne *et al*. 2002). It is accepted that the top 15–20 km of the crust behaves in a brittle-elastic fashion, facilitating the occurrence of large earthquakes. Two classes of model then apply for the remainder of the lithosphere. Lower crustal/upper mantle material beneath the upper crust might also be effectively rigid, resulting in a style of deformation involving fault-bounded tectonic blocks that is coherent throughout the entire lithosphere. This view has been put forward by Avouac *et al*. (1993) and Meade (2007) on the basis of GPS velocity fields and geological slip rates on major faults. In an alternative class of model, some portion of the lithosphere beneath the seismogenic upper crust has viscous properties that allow it to flow, with no pronounced localization of shear deformation beneath major faults in the upper crust. This view has been put forward in various forms by England & Molnar (1997), Houseman & England (1993), Royden *et al*. (1997), Zhang *et al*. (2004) and Bai *et al*. (2010), but how much of the lithosphere is weak enough to flow on subgeological time-scales, and at what depth, is still debated.

There are now many lines of geophysical evidence suggesting that the mid to lower crust in the northern part of the plateau is warm and weak enough to flow due to the presence of partial melts. This evidence ranges from high Poisson's ratio (Owens & Zandt 1997; Rodgers & Schwartz 1998), high seismic attenuation (Rodgers & Schwartz 1998; Fan & Lay 2003), high conductivity (Wei *et al*. 2001; Unsworth *et al*. 2004) and Quaternary volcanic rocks at the surface (Hacker 2000; Ding *et al*. 2003). Slow seismic velocities in the mantle beneath northern Tibet suggest that it is warmer than further south (Ni & Barazangi 1983; McNamara *et al*. 1997; Rapine *et al*. 2003), which may in part account for the especially warm lower crust. Several studies have also documented a change in conductivity across the Kunlun Fault (e.g. Wei *et al*. 2001; Unsworth *et al*. 2004, Rippe *et al*. 2010). In addition, the results of Unsworth *et al*. (2010) show a further decrease in conductivity across the southern margin of the Qaidam Basin. A thorough review by Klemperer (2006) details the results and interpretations of many geophysical studies of the Tibetan Plateau.

The occurrence of large earthquakes in this setting of thick, warm lower crust offers a relatively rare opportunity to probe crustal rheology using post-seismic relaxation. By contrast, in other tectonic settings where the crust is thinner and colder, the dominant post-seismic response to a large earthquake tends to occur in the mantle (e.g. Pollitz 2003a, 2005; Freed *et al*. 2006; Biggs *et al*. 2009). Determining an appropriate rheological model for Tibet is

© 2011 The Authors, *GJI*
Geophysical Journal International © 2011 RAS

important for understanding the geodynamics of the plateau. For example, loading of faults during the interseismic period would be expected to have a different evolution for different vertical rheology profiles. Equally, placing constraints on mechanical properties of the crust will inform efforts to understand the large-scale dynamics of how the plateau formed.

Savage (1990) showed that for an infinitely long vertical strike-slip fault, surface deformation due to distributed viscous flow in a Maxwell viscoelastic half space beneath an elastic upper crust can be matched exactly by a certain distribution of time-dependent fault slip at depth in an elastic half-space. For a finite-length, non-vertical strike-slip fault with variations in strike along its length, this equivalence does not apply, and vertical displacements are non-zero. However, when the finite-length fault is long compared to the depth of faulting, and near-vertical, it is possible to obtain very similar surface displacement fields for localised afterslip and distributed viscous flow at similar depths, and vertical displacements at the surface are small except near the rupture tips. For the case of Kokoxili, the length of fault that ruptured during the earthquake was ∼25 times the thickness of the seismogenic upper crust, and so there is large potential for ambiguity in inferences of rheological structure at depth made from observations of post-seismic motion at the surface. Ryder *et al*. (2007) found such ambiguity for the case of the 1997 Manyi earthquake, which ruptured a fault only 12 times longer than the thickness of the upper layer.

1.2 Previous coseismic and post-seismic studies of the 2001 Kokoxili earthquake

Coseismic displacements for the 2001 November 14 Kokoxili earthquake have been investigated using both InSAR (Lasserre *et al*. 2005) and GPS (Wang *et al*. 2003). Lasserre *et al*. (2005) used InSAR data and solved for distributed slip, assuming a pure left-lateral sense of motion, and estimated a maximum offset of about 8 m, with 3–4 m of slip occurring down to a depth of 10 km at certain places along the vertical fault. For their analysis of GPS data, Wang *et al*. (2003) assumed depth-uniform slip on each of 16 fault segments along strike, but allowed the rake on each segment to vary. They estimated up to a maximum of 5.35 m of strike slip, with an increasing amount of dip slip, up to 1.14 m towards the east. The depth of slip in their model is 16.5 km, but the authors point out that the actual depth of coseismic slip may be less than this since their GPS data set included 4 months of post-seismic displacement. Shen *et al*. (2003) modelled 6 months of post-seismic GPS data for the Kokoxili earthquake, and inferred that both afterslip and viscoelastic relaxation in a lower crustal weak layer occurred. The thickness of the viscoelastic layer in the model was 20 km and the Maxwell viscosity was 5×10^{17} Pa s. Ren & Wang (2005) used the same GPS sites as Shen *et al*. (2003) but had longer time-series lasting 1 yr. They noted that about 50 per cent of the total observed surface deformation (3 weeks to 1 yr) occurred during the first two observation weeks, that is, the deformation rate was very rapid initially and decreased over time.

1.3 This study

In this study, we use the post-seismic response of the Kokoxili earthquake to investigate the physical properties of the thick Tibetan crust. Since the top of the upper mantle is deep here (>55 km), any time-dependent surface motion will be sensitive mainly to the properties of the crust, with the mantle having only a minor influence. We present post-seismic GPS and InSAR data for the first five years following the Kokoxili earthquake. The GPS measurements cover the first year, starting 13–19 days after the earthquake, and the InSAR data cover years two to five. We start by considering models of stress relaxation by viscous flow in the mid to lower crust, and explore what rheological properties reproduce the data satisfactorily. Initially, the effects of viscoelastic layering on the spatial displacement field are investigated. Then, following on from the conclusion of Ryder *et al*. (2007) that the effective viscosity of the lower crust increased over time following stress loading by the nearby Manyi earthquake, we utilize a biviscous rheology with two material relaxation times (Pollitz 2003a, 2005). It should be noted that a power-law medium predicts a decrease in effective viscosity at the time of the earthquake itself, after which the effective viscosity increases as stress changes are relaxed. Afterslip models are run to assess to what extent a model of deep slip can explain the observations. We also apply the optimal viscoelastic model to the Manyi post-seismic data set of Ryder *et al*. (2007) to assess the variability in rheological structure along the western end of the Kunlun fault system.

2 DATA

2.1 GPS data

We use post-seismic GPS data along a transect crossing the fault obliquely in its eastern half (Fig. 1), as presented by Ren and Wang (2005). The sites were first occupied post-seismically between 1 and 3 months following the earthquake, and the time-series run until the end of 2002 November, that is, about a year after the mainshock. These early time-series are invaluable because they cover most of the time between the earthquake and the start of the InSAR dataset in early 2003. A regional velocity field representing interseismic deformation was obtained from pre-earthquake GPS data and removed from the time-series (Shen *et al*. 2003). Fig. 2 shows horizontal displacements for each site between 2001 December and 2002 November.

2.2 InSAR data

2.2.1 Post-seismic interferograms

To construct interferograms of surface deformation, we make use of SAR data from the European Envisat satellite from early 2003 until early 2007. All data were processed using the open source ROIPAC software developed at Caltech/JPL (Rosen *et al*. 2004), using the 90 m SRTM DEM to correct for topographic phase. Unwrapping was carried out using the branch cut algorithm within ROIPAC. The InSAR data set as a whole shows good coherence over the western part of the rupture area. Coherence is not as good over the eastern half, the main reason being the high relief of the Kunlun Shan in the eastern part of the study area, which gives rise to geometrical decorrelation and tropospheric water vapour artefacts. A subset of the interferograms was selected for use in the present analysis (Table 1), based on their relatively high coherence values and low contributions of topography-correlated noise due to tropospheric water vapour. By way of example, Fig. 3 shows two post-seismic interferograms, one on descending track 405 and the other on ascending track 355 (see Fig. 1 for locations). The ascending interferogram has the sign of range change on either side of the fault reversed with respect to the descending interferogram,

© 2011 The Authors, *GJI*
Geophysical Journal International © 2011 RAS

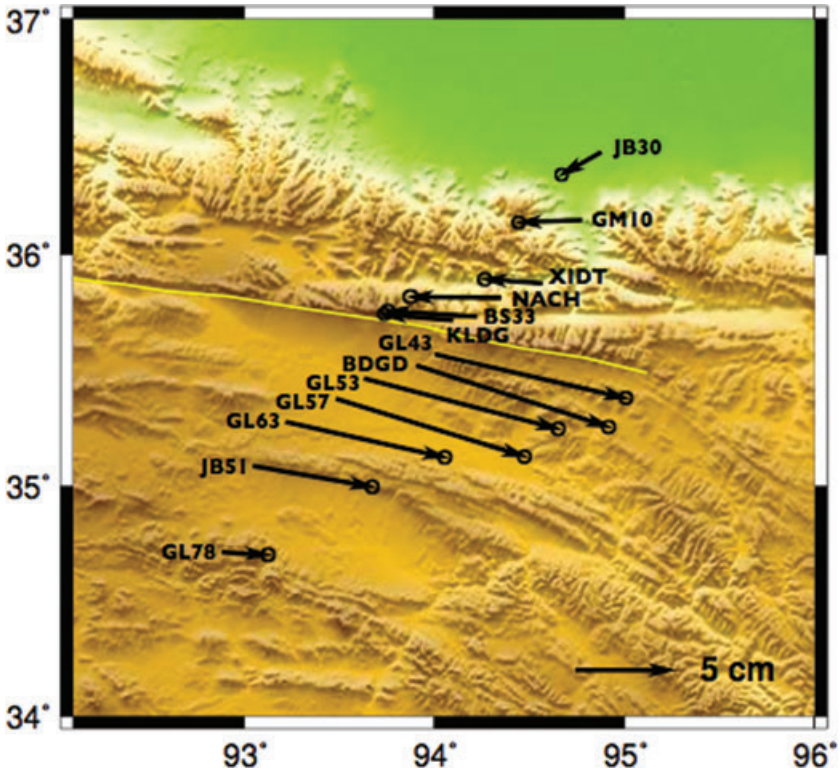

Figure 2. Horizontal GPS displacements between 2001 December and 2002 November.

Table 1. Details of post-seismic interferograms shown in Figs 3 and 4, and in Fig. 10 as profiles. Start and end dates are given in yyyy/mm/dd format.

Figure(s)	Track	desc/asc	Start	End	Years	B_{perp} (m)
3, 4, 10	405	desc	2003/12/23	2004/12/07	0.97	12
3, 10	355	asc	2005/01/12	2007/01/11	1.92	46
4	176	desc	2003/12/07	2004/12/26	1.05	360
10	176	desc	2004/11/21	2005/12/11	1.06	36
4, 10	362	desc	2003/10/11	2004/10/30	1.05	49
4	448	desc	2004/03/05	2004/12/10	0.76	37
4	90	desc	2003/10/27	2004/10/11	0.96	61

indicating that displacements are mostly horizontal, as expected for a long strike-slip fault. The sense of offset across the fault is left-lateral, which is the same as the coseismic sense. Fig. 4 is a collage of interferograms on different tracks that cover approximately the same period of time (2003–2004). Details of the interferograms are given in Table 1. Note that the line of sight vector varies across each SAR track, and the variation in start/end dates for the group of interferograms is up to about 3 months. The first-order pattern of line of sight deformation is very similar to that for the 1997 Manyi earthquake (Ryder *et al*. 2007), which had a similar fault strike and a predominantly left-lateral sense of slip. In both cases, the pattern of descending line of sight displacement consists of an elongate lobe of positive range change on the north side of the fault and an elongate lobe of negative range change south of the fault (compare Fig. 4 of this paper and fig. 2 of Ryder *et al*. (2007)).

2.2.2 Post-seismic time-series

To gain an idea of the temporal decay of post-seismic stress relaxation, 15 interferograms on Track 176 were used to construct a time-series. Track 176 was the most coherent of all the tracks over the entire observation period (2003–2007), and was the only track with enough interferograms to allow time-series inversion. The method followed is the same as that described in Ryder *et al*. (2007) for producing the Manyi post-seismic time-series, and so is described only briefly here. The line of sight displacement in each interferogram is used on a pixel-by-pixel basis, along with the known start and end dates of each interferogram, to invert using smoothed least squares for cumulative displacements relative to a reference time (the earliest start date of the set of interferograms). The smoothing applies a weighted constraint that velocities in adjacent time windows should be constant. For the resulting time-series shown in Fig. 5, the reference date is 2003 April 6 and the time-series extends until 2006 November 26. Line of sight displacements are shown for all dates on which a SAR acquisition was made, and the plot at bottom right shows the mean absolute pixel displacement from the entire deforming area as a function of time. This curve may be compared with the earlier GPS time-series in Fig. 9.

3 MODELLING OF VISCOELASTIC RELAXATION

3.1 Objectives

The aim of modelling the geodetic data is to constrain the rheological structure of the crust in this part of Tibet, including the thickness of any distinct rheological layers as well as their elastic and viscous properties. For the purposes of this paper, the term lower crust refers to the part of the crust beneath the elastic upper crust in which earthquakes occur, that is, between about 20 and 55 km. For modelling surface displacements due to

© 2011 The Authors, *GJI*
Geophysical Journal International © 2011 RAS

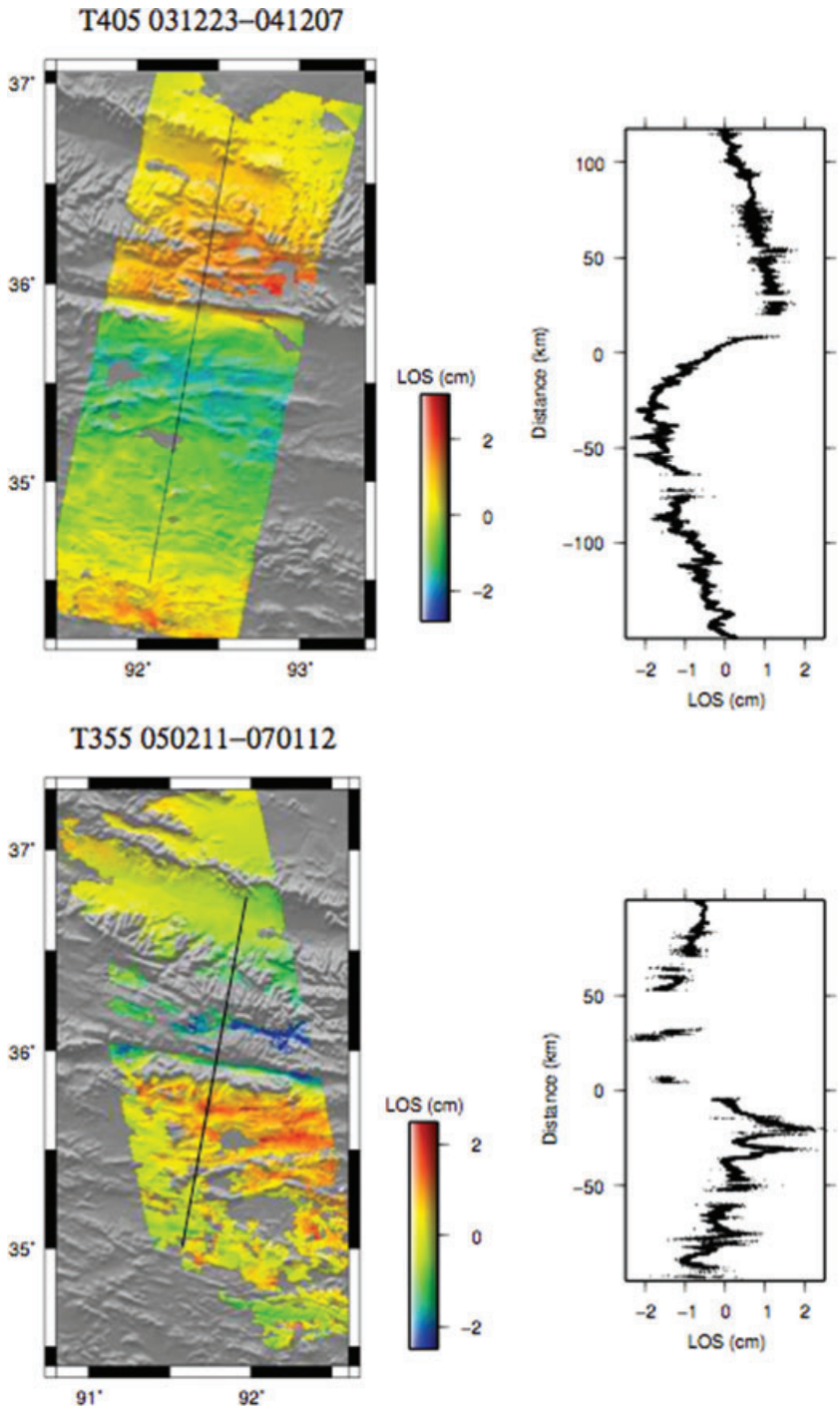

Figure 3. Post-seismic Envisat interferograms for Track 405 (descending) and Track 355 (ascending). Dates given above each interferogram are start and end date, with the format yymmdd. Black lines mark positions of line of sight displacement profiles shown beside the interferograms.

viscoelastic relaxation in the lower crust, we start by assuming a radially symmetric earth with distinct elastic and viscoelastic layers, using the Fortran code VISCO1D (Pollitz 1992). The parameters to be constrained are: (i) the thickness of the viscoelastic layer(s) in the lower crust, and (ii) the mechanical properties of the layer(s), in particular viscosity. In the Discussion, we briefly consider the effects of lateral heterogeneity in material properties across the southern margin of the Qaidam Basin, and we test whether the results obtained for the Kokoxili area also apply to the Manyi area.

3.2 Viscoelastic stratification in the crust

Before modelling the time dependence of the observed post-seismic signal, we focus on the spatial displacement pattern to gain an idea of the main layering in the crust. Since the displacement pattern (as opposed to the temporal response) depends primarily on the configuration of layers rather than their mechanical properties, our initial aim is to broadly reproduce the two-lobe pattern seen in the collage of Fig. 4 by specifying Maxwell viscoelastic layers in the crust. Although Ryder *et al*. (2007) showed that a Maxwell

© 2011 The Authors, *GJI*
Geophysical Journal International © 2011 RAS

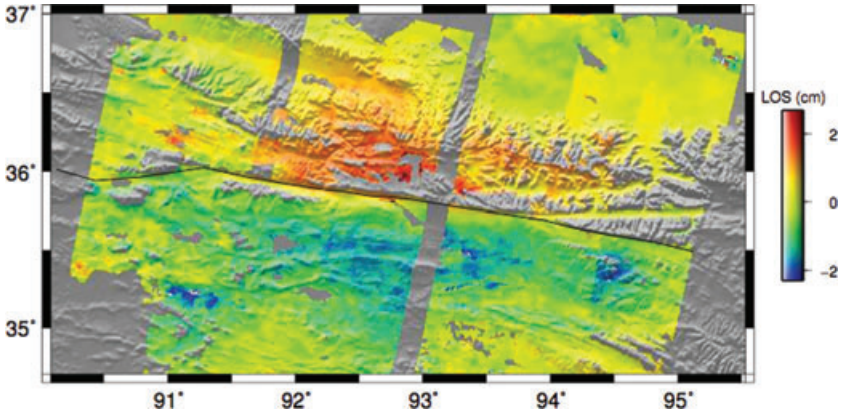

Figure 4. Collage of post-seismic descending interferograms that all have start/end dates within a few months of each other. Dates for each interferogram are given in Table 1.

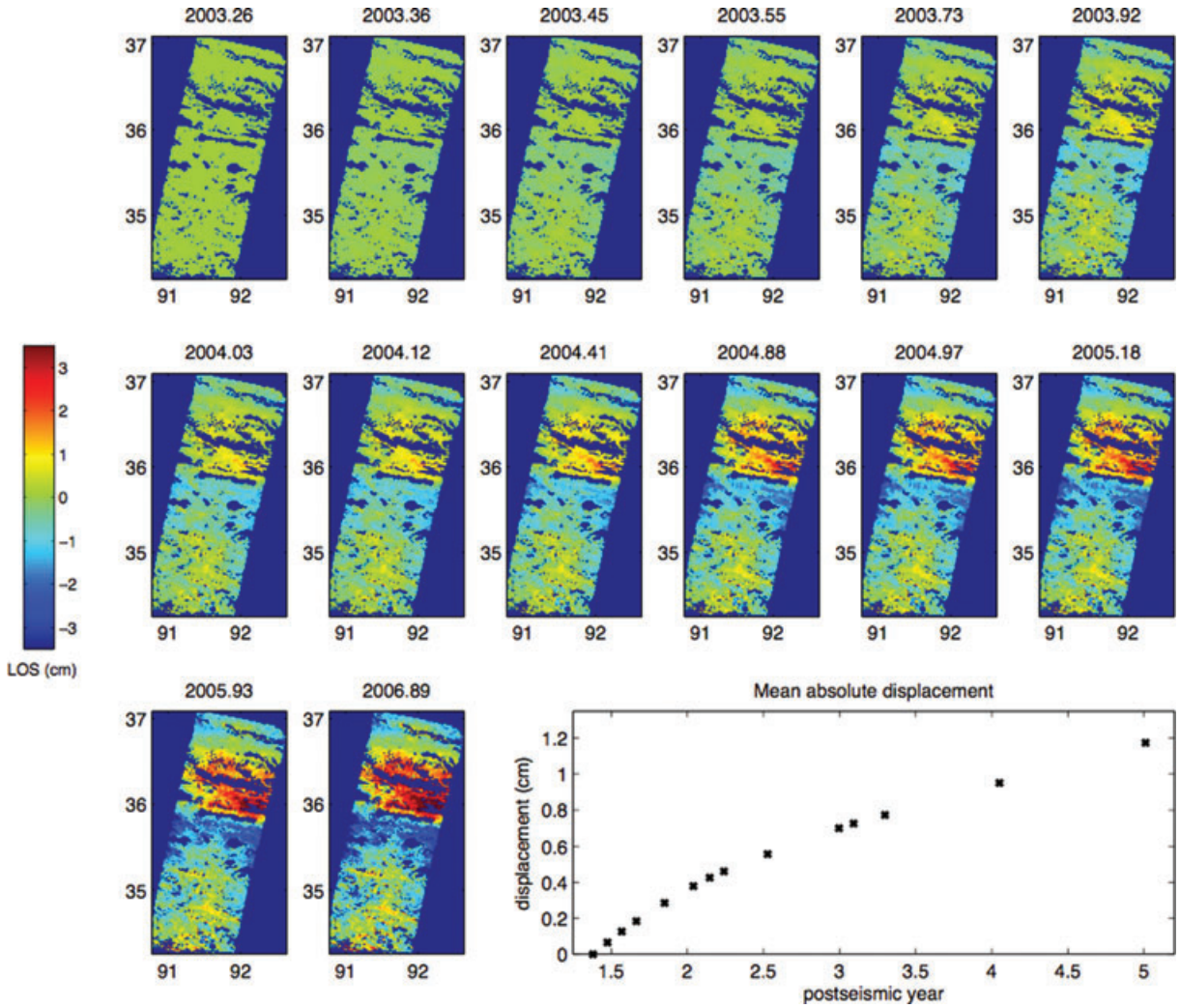

Figure 5. Time-series for Envisat Track 176. Line of sight displacements are referenced to the first date, which is 2003 April 6. The lower right plot shows the mean absolute displacement of all pixels in the deforming area as a function of time.

rheology does not fit the time dependence of the observed post-Manyi earthquake deformation, choosing a Maxwell rheology is sufficient for this exercise because the spatial pattern looks very similar whether a Maxwell or Burgers (or standard linear solid) rheology is implemented.

We model two viscoelastic crustal layers beneath an elastic upper crust, varying the thickness of the upper viscoelastic layer (d) and the viscosity ratio between the upper and lower layers (γ). The lower layer is set to be many times the thickness of the upper crust. The coseismic slip model used as input into the viscoelastic models is

© 2011 The Authors, *GJI*
Geophysical Journal International © 2011 RAS

Table 2. Coseismic slip parameters obtained by Wang *et al*. (2003) from GPS data and used as input into the viscoelastic models.

Segment	Western end lon	Western end lat	Eastern end lon	Eastern end lat	Strike slip (m)	Dip slip (m)
1	90.130	36.010	90.431	35.940	−0.14	0.25
2	90.431	35.940	90.783	35.963	−2.05	0.19
3	90.783	35.963	91.285	36.022	−2.61	0.67
4	91.285	36.022	91.611	35.966	−1.54	0.00
5	91.611	35.966	91.896	35.923	−1.80	0.04
6	91.896	35.923	92.211	35.884	−2.12	0.14
7	92.211	35.884	92.372	35.870	−2.29	−0.07
8	92.372	35.870	92.584	35.843	−3.78	0.04
9	92.584	35.843	92.912	35.820	−5.21	0.16
10	92.912	35.820	93.277	35.773	−3.89	−0.52
11	93.277	35.773	93.661	35.726	−5.35	−0.46
12	93.661	35.726	93.946	35.691	−3.23	−0.25
13	93.946	35.691	94.167	35.646	−3.12	−1.14
14	94.167	35.645	94.459	35.598	−2.47	−1.07
15	94.459	35.598	94.795	35.556	−2.49	−0.37
16	94.795	35.556	95.120	35.490	−1.34	0.04

Table 3. Values of upper viscoelastic layer thickness (d) and viscosities (η_1, η_2) used in the spatial modelling of Section 3.2. The parameter γ is the ratio of η_1 to η_2.

d	10, 25, 50 km				
γ	0.01	0.1	1	10	100
η_1 (Pa s)	10^{17}	10^{18}	10^{19}	10^{19}	10^{19}
η_2 (Pa s)	10^{19}	10^{19}	10^{19}	10^{18}	10^{17}

the depth-uniform, variable-rake slip model of Wang *et al*. (2003), whose parameters are listed in Table 2. This GPS-derived model is preferred over the InSAR-derived model of Lasserre *et al*. (2005), since the InSAR data set only has good spatial coherence in the easternmost track, and so the slip distribution west of about 93° is poorly constrained. We fix the thickness of the upper crust at 16.5 km, which is the optimal depth of coseismic slip estimated by Wang *et al*. (2003), and is also consistent with the model of Lasserre *et al*. (2005). Making the elastic upper crust in the model either thicker or thinner leads to the fault-perpendicular wavelength of the post-seismic deformation pattern being over-predicted or under-predicted, respectively. The vertical fault assumed in the Wang *et al*. (2003) model is consistent with the results of a careful analysis of body wave seismograms by Robinson *et al*. (2006), who determined a dip of 90° for the part of the Kunlun Fault that ruptured. As stated above, the GPS data set used by Wang *et al*. (2003) extends to the fourth post-seismic month. Although this may mean that the nominally coseismic slip obtained in their inversion is slightly over-estimated, this bias is moderated by their inclusion of surface offset measurements across the fault carried out immediately after the earthquake. Any afterslip that is nonetheless estimated as part of the coseismic slip distribution will add to driving the viscoelastic relaxation.

Three values of d are tested (10, 25 and 50 km) and five values of γ (0.01, 0.1, 1, 10, 100). Since the best-fit viscosity of the geodetic data sets using a Maxwell half space is 10^{19} Pa s, this value is applied to the upper layer when $\gamma > 1$ and the lower layer when $\gamma < 1$. The combinations of d and γ tested are given in Table 3. The grid in Fig. 6 shows predicted line of sight displacements for the 15 different combinations of d and γ. For the low γ cases, the displacement lobes on both the southern and northern sides become more bulbous towards the east, which is not observed in the InSAR collage. In addition the lobes are broader in a cross-fault direction than is observed (compare the InSAR collage in Fig. 4). For the high γ cases the pattern is again too broad, and the models predict a quadrant pattern of positive and negative range change, which is not observed. In contrast, the $\gamma = 1$ case gives two more equal lobes on the north and the south side, very similar to the InSAR collage, and the lobes have a similar width to those observed. Since the viscosities of the upper and lower layers are the same, this model is equivalent to a viscoelastic half-space beneath the elastic upper crust. We also tested γ values slightly larger and greater than unity, and found that the viscosity of the two layers could change by up to

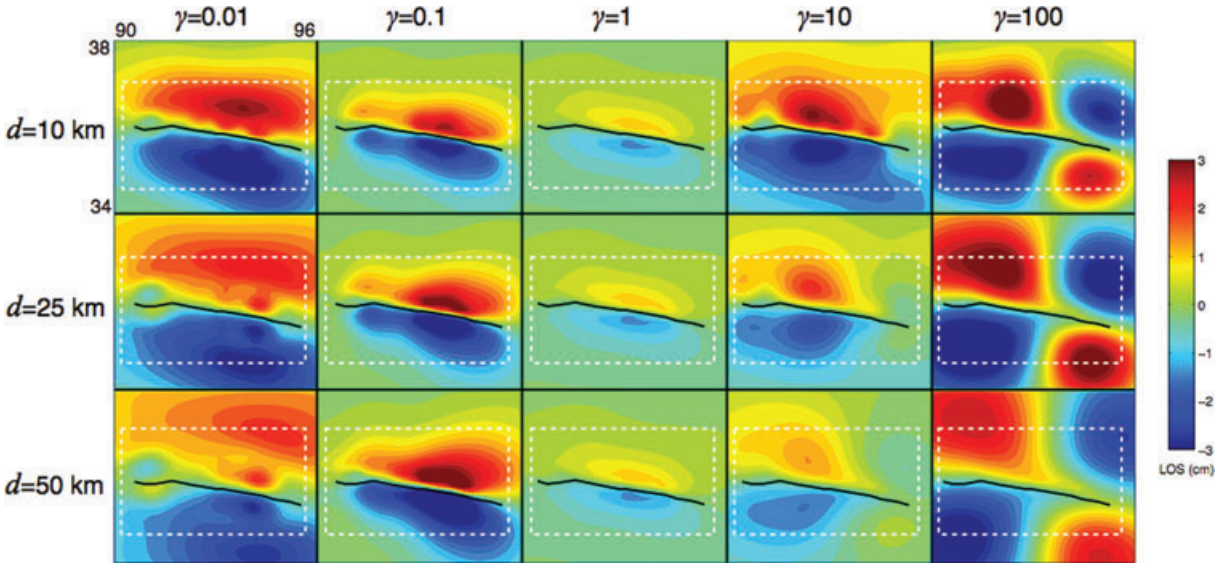

Figure 6. Line of sight displacements predicted by models with two Maxwell viscoelastic layers (lower layer is very thick) below a 16.5 km-thick elastic lid. An Envisat descending viewing geometry is assumed. The viscosity ratio of the upper and lower layers is represented by the parameter γ, while the thickness of the upper viscoelastic layer is represented by the parameter d. Values of these two parameters are given above/beside the grid. White dashed boxes represent the area covered by the interferogram collage in Fig. 4.

© 2011 The Authors, *GJI*
Geophysical Journal International © 2011 RAS

a factor of about three before the spatial pattern started departing from the observed pattern. We therefore conclude that there is no major resolvable stratification of viscoelastic layers in the crust, but rather that the crust is fairly homogeneous in its properties.

3.3 Modelling time dependence with a Burgers rheology

For the 1997 Manyi earthquake, Ryder *et al*. (2007) showed that a Maxwell rheology with a single decay constant cannot explain the first four years of InSAR observations. Similarly, modelling of the Kokoxili early GPS time-series with a Maxwell half space beneath an elastic upper crust under-predicts the initial transient displacements and over-predicts later displacements. We therefore assign a Burgers rheology for the crust beneath the seismogenic upper crust. This transient rheology is represented mechanically by a Kelvin element in series with a Maxwell element. The Kelvin element consists of an elastic component with shear modulus μ_1 in parallel with a viscous component with viscosity η_1. The Maxwell element consists of an elastic component with shear modulus μ_2 in series with a viscous component with viscosity η_2. When this composite is subjected to a stress which is held constant after being imposed, only the elastic component of the Maxwell element strains instantaneously; subsequently, the Kelvin and Maxwell elements experience strain, at rates determined by their viscous components. Eventually the Kelvin element ceases to strain and steady-state strain is achieved by the Maxwell element alone. Thus, there is a transient period of strain whose strain rate is determined by the Kelvin element, followed by a steady-state period of strain. During the transient period, the shear modulus of the entire system relaxes from its initial instantaneous, Maxwell value, μ_2 to a long-term value, μ', which is equal to $\mu_1\mu_2/(\mu_1+\mu_2)$. In this study, the relaxation of the shear modulus is parameterized by α, defined as the ratio of the long-term to the initial shear modulus, $\alpha = \mu'/\mu_2$.

The aim of the Burgers rheology modelling is to estimate η_1, η_2 and α, and also to estimate the depth at which viscoelastic relaxation occurs, with the thickness of the viscoelastic layer being parameterised by the variable h. Material below this layer is given a very high viscosity, such that its relaxation time is too long to result in any significant creep response over the timescale of interest. For each data set, a coarse 3-D grid search over $\eta_1/\eta_2/\alpha/h$ parameter space is carried out. The value of η_1 is varied between 10^{16} and 10^{19} Pa s, and η_2 is varied between 10^{17} and 10^{20} Pa s, both in order of magnitude steps; α is varied between 0.46, corresponding to 54 per cent relaxation of shear modulus during the transient period and 0.92, corresponding to 8 per cent relaxation in five equal steps. The viscoelastic layer thickness h is given values of 16, 40, 65 and 100 km, and also a half-space is simulated by making h very large. The Moho depth in this part of the plateau is estimated to be about 55 km (Owens & Zandt 1997), so for an upper crustal thickness of 16 km, the 40 km thick layer case is equivalent to the entire lower crust being viscoelastic.

For all nodes on the grid search, a root mean square (rms) misfit between model and data is calculated. Once the optimal node of parameter space has been determined in a coarse sense, a finer grid search is carried out in the vicinity of this node. Hereafter, an individual node in parameter space is denoted $\{\eta_1/\eta_2/\alpha/h\}$, where the terms are as defined above and the units are Pascal-second for the two viscosities and kilometres for the layer thickness.

3.4 Coarse grid search

For the GPS data set, the optimal node for the coarse grid search is at $\{10^{18}/10^{19}/0.69/65\}$. Fig. 7(a) shows misfit as a function of η_1 and η_2 for the optimal values of α and h. The misfit is only weakly sensitive to η_1 but is very sensitive to η_2. This is because it

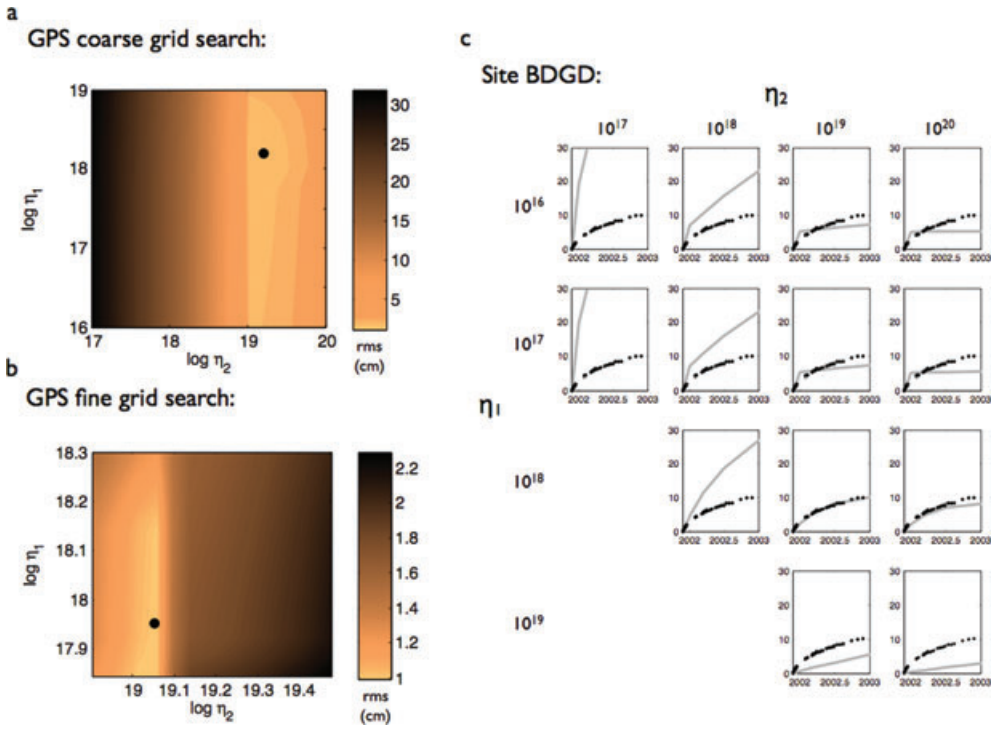

Figure 7. Rms misfits between GPS data and model predictions as a function of the transient and steady-state viscosities η_1 and η_2, for the coarse (a) and fine (b) grid searches. The shear modulus ratio (α) is 3:2 and thickness of the single viscoelastic layer (*h)* is 65 km. The series of curves in (*c*) shows the time-series for southern site BDGD (see Fig. 1 for location) and the modelled curve for various combinations of viscosities.

© 2011 The Authors, *GJI*
Geophysical Journal International © 2011 RAS

is the steady-state viscosity η_2 that controls the overall magnitude of surface motion, and so for a given value of η_2 there is not much variation in η_1. The strong lower bound and weak upper bound on η_2 (at this coarse grid resolution) is a results of the decrease from very large to small displacements as η_2 increases. The time-series shown in Fig. 7(c) are for site BDGD on the south side of the fault (see Fig. 1 for location) and demonstrate the effect on the relaxation curve of different combinations of η_1 and η_2. If the steady-state viscosity is over an order of magnitude greater than the transient viscosity, then the modelled time-series flattens off too quickly after the first few months. Conversely, as the two viscosity values approach each other, then a Maxwell rheology is approximated, and the modelled curves are too linear to explain the rapid early displacement rate and the subsequent slower rate. The greatest effect of changing α is to alter the magnitude of strain at any particular point; the effect on time dependence is much less significant, this being chiefly determined by the viscosity values, including the ratio between viscosities. The value of α is therefore rather well constrained; for example, relative to the optimal model parameters obtained, a lower value of α—that is, lower long-term strength—gives a greater magnitude of displacement, but increasing viscosities to compensate for this alters the curvature of the decay curve such that it no longer matches the measured time-series.

For the InSAR data set, rms values are computed by averaging line of sight displacements across a 1°-wide swath centred on the model profile line. The coarse grid search yields optimal values of $\{10^{19}/10^{19}/0.69/16\}$. Misfit plots are shown in Fig. 8, both for $h = 16$ km and $h = 65$ km, the latter being the optimum value of h obtained in the GPS grid search. As for the GPS results, the misfit at the minimum in η_2 varies by only a very small amount across three orders of magnitude in η_1. For the $h = 65$ km case, the material parameters are the same as for the GPS case, that is, $\{10^{18}/10^{19}/0.69\}$.

3.5 Fine grid search

Because the InSAR profiles post-date the earthquake by two or more years, the fine grid search is carried out only for the GPS data set. The value of η_1 is varied between 7×10^{17} and 2×10^{18} Pa s, and η_2 is varied between 8×10^{18} and 3×10^{19} Pa s; α is varied between 0.62 and 0.76. The range of h is retained from the coarse grid search. The optimal node is at $\{9\times10^{17}/1\times10^{19}/0.69/65\}$, for which the residual is 1.04 cm. As for coarse grid search, the misfit is more sensitive to η_2 than to η_1. Note that the finer grid resolution gives a steeper increase in misfit at higher η_2 values, relative to the coarse grid resolution. In Fig. 9 the time-series for each GPS site is plotted along with the prediction of our optimal Burgers model. Close inspection of this figure reveals that while the model predicts displacements for sites to the south of the fault very well, with the exception of site GL43 immediately south of the fault, which is under-predicted, displacements are over-predicted by up to 100 per cent for the four northernmost sites. For the thinnest viscoelastic layer case, $h = 16$ km, the data-model misfit is 8 mm greater than for the optimal case, so a mid-crustal viscoelastic channel scenario can be ruled out. The misfits for the 40 km-thick layer case, which corresponds to the entire crust being viscoelastic, and the 100 km-thick layer case are both just over 1 mm greater than for the 65 km-thick layer case. The data therefore do not allow us to distinguish between these three scenarios, and our interpretation is that stress relaxation by viscous flow occurs at least throughout the entire crust, and possibly extends into the upper mantle.

As a check on the results obtained from the GPS data, Fig. 10 shows line of sight displacements perpendicular to the fault for four of the interferograms listed in Table 1, along with the predictions of the optimal Burgers model derived from the GPS fine grid search. InSAR displacements are shown for pixels within 0.5° either side of the nominal model profile line. Since we expect interseismic motion to contribute to the range change pattern of the interferograms, our post-seismic model profiles are adjusted by adding an interseismic component, $u_{\text{interseismic}}$, using the formulation given in Savage & Burford (1973):

$$\mu_{\text{interseismic}} = \frac{V}{\pi} \tan^{-1}\left(\frac{x}{D}\right), \tag{1}$$

where V is the relative far-field plate velocity, D is the locking depth and x is the distance from the fault. We use a value for V of 10 mm yr^{-1} (Haibing *et al*. 2005) and a locking depth of 16.5 km. The interseismic component is represented by the dashed lines in Fig. 10. Both the wavelength and the magnitude of the post-seismic deformation are well matched by the model for all four interferograms. There is a small degree of north–south asymmetry

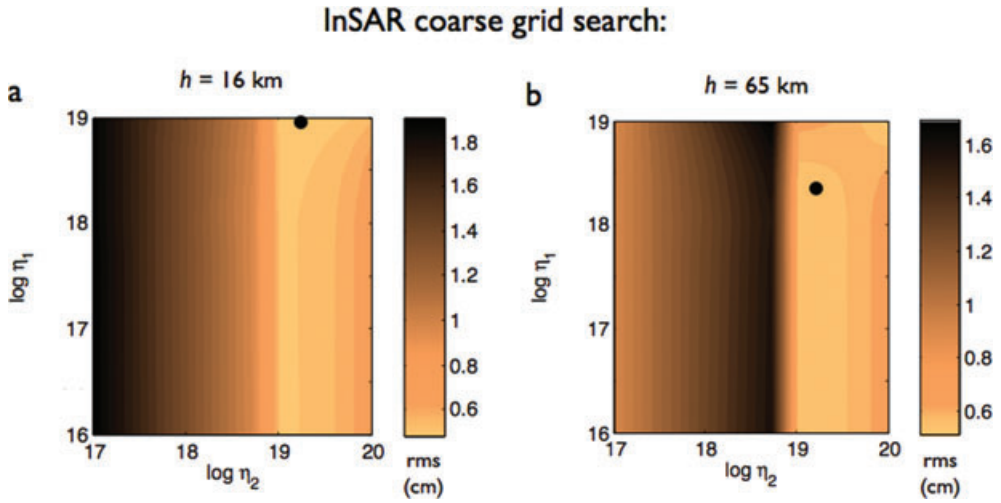

Figure 8. Rms misfits between InSAR line of sight displacements and model predictions as a function of η_1 and η_2. Misfits are computed using average line of sight displacements across a 1°-wide swath (see Fig. 10 for displacement profiles). Results for both $h = 16$ km (a) and $h = 65$ km (b) are shown. The shear modulus ratio is 3:2 in both cases.

© 2011 The Authors, *GJI*
Geophysical Journal International © 2011 RAS

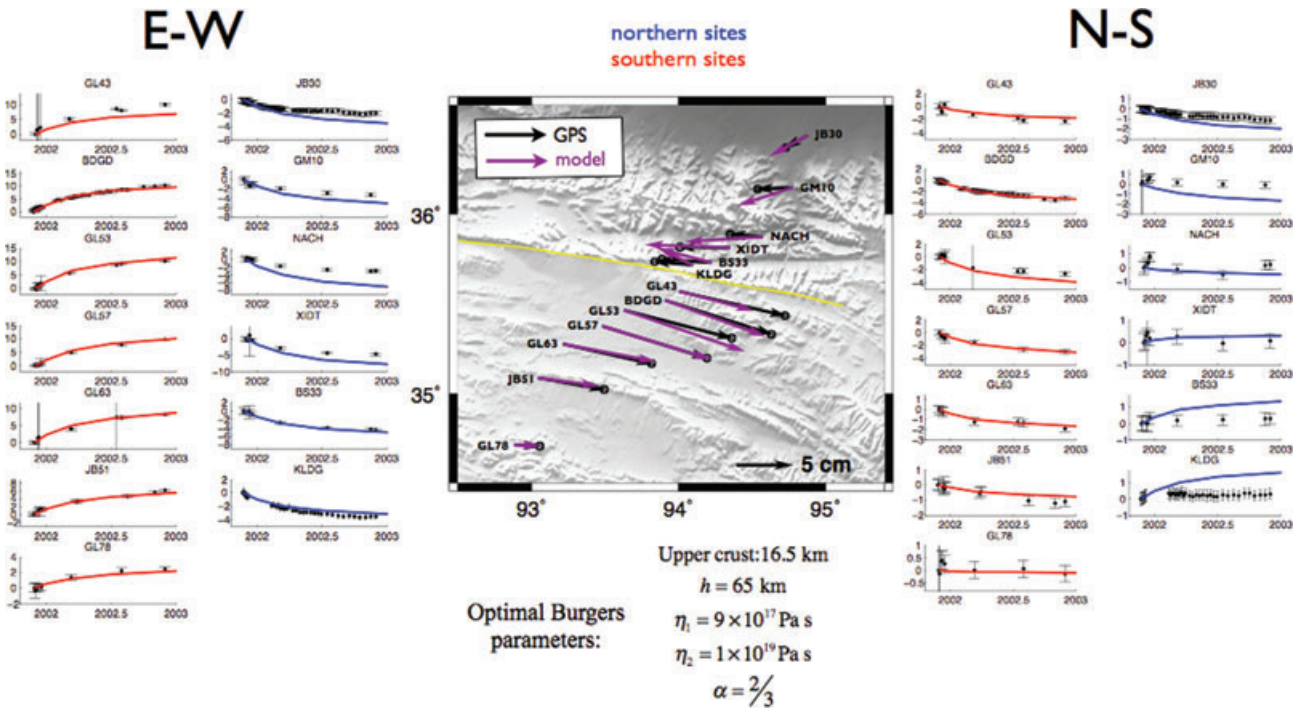

Figure 9. Left and right: GPS time-series (black dots) with predictions of optimal Burgers model (continuous lines). Year is on horizontal axis and displacement in centimetres is on vertical axis. Red lines denote GPS sites south of the fault and blue lines denote sites north of the fault. GPS displacements between 2001.9 and 2003 (black arrows) are shown in the centre plot, along with the modelled displacements (cyan arrows).

in the extent to which the modelled profiles fit the InSAR profiles, evident for tracks 176, 362 and 355. Similar to the GPS case, the model over-predicts displacements on the northern side.

4 AFTERSLIP MODELLING

Afterslip is another plausible mechanism for how stress changes induced by an earthquake might be relaxed (e.g. Hearn *et al*. 2002, Johnson *et al*. 2006, Bürgmann & Dresen 2008, Ryder *et al*. 2010). In this case, the relaxation occurs by aseismic slip on a localized shear zone that is usually considered to be an extension of the fault plane at depth, though slip may also occur on parts of the shallower rupture zone. Since the GPS data set, which covers the first year, does not have sufficient spatial coverage of the fault to allow a robust inversion for afterslip during this early time interval, we consider the later time interval covered by the InSAR collage (2004), inverting for afterslip on the coseismic fault plane and its extension at depth down to well beneath the bottom of the crust. The general methodology follows that described in Ryder *et al*. (2007) in their study of the 1997 Manyi earthquake, although here we invert data for a single time window, rather than inverting different stages of a time-series. Since the start/end dates of the five interferograms in the collage (Fig. 4) are slightly staggered, we use the time-series shown in Fig. 5 to scale the individual interferograms to the Track 405 time interval (2003 December 23–2004 December 07) according to the temporal decay curve. Slip is allowed to occur from the surface down to a depth of 70 km, which is 15 km deeper than the estimated crustal thickness in this part of the Tibetan Plateau. The 16-segment fault geometry of Wang *et al*. (2003) is used, as for the viscoelastic modelling, and each segment is discretized into seven depth patches. Initially, the rake is assumed to be 0° (pure left-lateral slip) for all patches. A non-negative constraint and Laplacian smoothing are applied, and the data are weighted using an estimate of correlated noise in non-deforming regions to compute a variance–covariance matrix for each interferogram. The same correlated noise parameters are also used to estimate the errors in the obtained afterslip distribution using Monte Carlo iteration (see Ryder *et al*. (2007) for further details).

The results of the afterslip inversion are shown in Fig. 11. We note that the slight reduction in slip magnitude on the segment about half way along the fault is likely an artefact resulting from the small gap in the InSAR collage at this point. The inversion places most of the slip between depths of 20 and 50 km. A small amount of slip is located above this zone (10–20 km) and beneath this zone (50–70 km), and negligible slip is seen from the surface down to a depth of 10 km. This depth distribution implies that the post-seismic relaxation process(es) mostly occurred in the mid to lower crust. The maximum inferred slip is 18 cm, and the total moment release over the ∼1 yr observation period is 6.47×10^{19} N m, which is equivalent to a M_w 7.1 earthquake. It should be noted that the rate of relaxation would have been significantly faster immediately following the earthquake, and so the total cumulative moment release up to the end of 2004 would have been much greater.

The slip model gives a reasonable first-order fit to the InSAR collage, although the wavelength of the displacement field is slightly less than observed. Horizontal displacements were also forward modelled for the 13 GPS sites (Fig. 12), with the displacement vectors being upscaled empirically to allow for the earlier time window of the GPS relative to the InSAR data. The azimuths of the modelled vectors do not match those of the measured vectors, being more oblique to the fault strike. We therefore allowed the rake to vary between ±45 from pure left-lateral in the InSAR inversion, but since this allowed a component of dip-slip, the GPS vectors were then even more oblique to the fault.

© 2011 The Authors, *GJI*
Geophysical Journal International © 2011 RAS

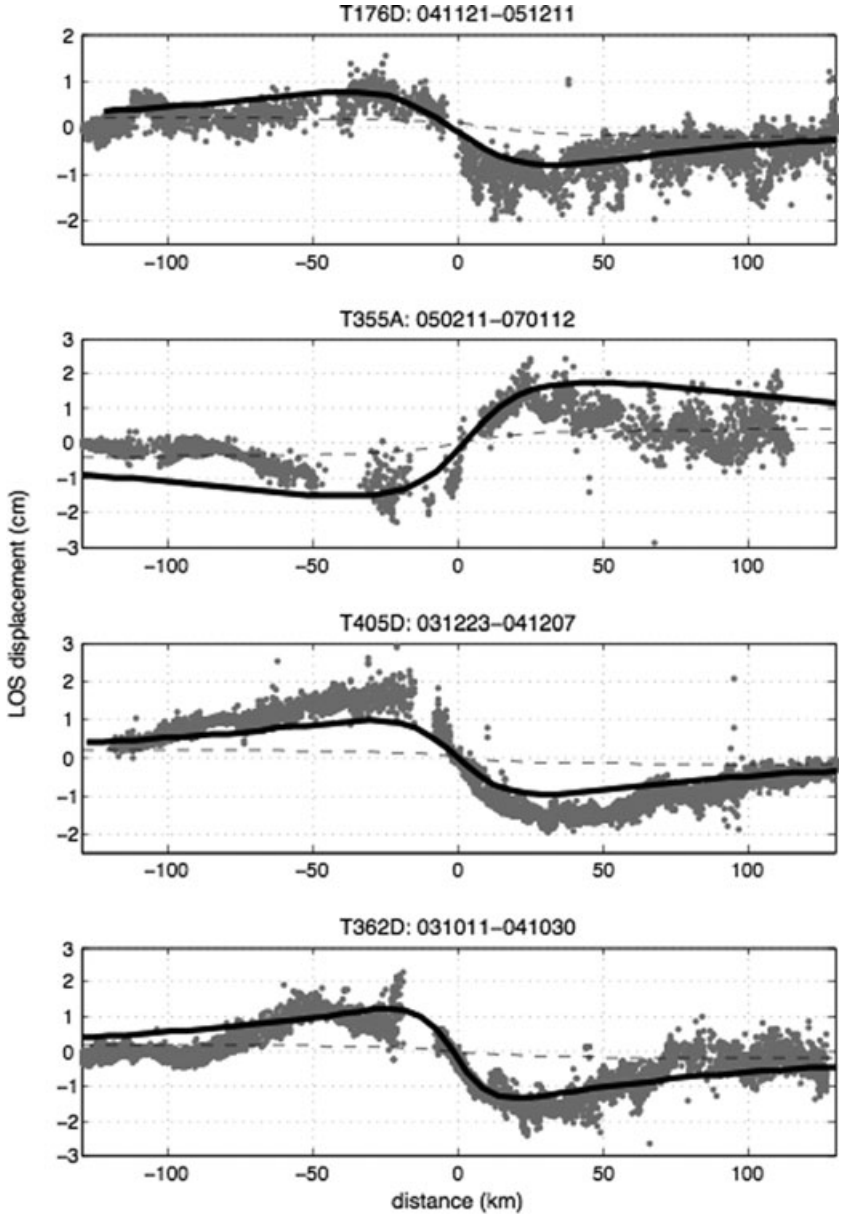

Figure 10. InSAR line of sight displacements (grey dots) along profiles across the fault, with optimal Burgers model predictions shown by black lines. Observed displacements from all points within 0.5° either side of the nominal profile line are shown. Thin dashed lines show modelled interseismic motion.

To further investigate this discrepancy in GPS vector azimuths, we inverted a synthetic viscoelastic displacement field for afterslip. The line of sight displacements from the Maxwell viscoelastic half space model in Section 3.2 (Fig. 6, top middle) was used as the 'data' vector in the inversion. The resulting slip distribution was forward modelled to produce both horizontal displacement vectors and line of sight displacements (Fig. 12). The top right plot demonstrates that although the returned lobe pattern of the line of sight displacement field matches the input well in a visual sense, there is some discrepancy in the azimuths of the vectors. In the southeastern quadrant, the 'modelled' vectors are systematically too clockwise of the 'data' vectors, as is seen in the inversion of the real InSAR data. There is also some mismatch in the northeastern quadrant, though not as pronounced. This synthetic test supports the conclusion that the post-seismic deformation seen in the InSAR data set is at least partially a result of viscous flow in the lower crust.

5 DISCUSSION

5.1 Contribution of afterslip to post-seismic relaxation

Afterslip has been inferred to occur following several earthquakes in different tectonic settings (e.g. Hearn *et al*. 2002, Jacobs *et al*. 2002, Ryder *et al*. 2010). Although the first-order features of the GPS/InSAR post-seismic data set for the Kokoxili earthquake can be explained very well by viscoelastic relaxation in a Burgers lower crust, afterslip would be expected at least in the zone immediately down-dip of the coseismic rupture, in the transition from brittle to ductile behaviour, and the top of the viscoelastic layer may in fact be deeper than 16.5 km. End-member afterslip modelling demonstrates that slip at much greater depths (20–50 km) beneath the coseismic fault plane can give a reasonable match to the InSAR displacements during the 2004 observation period, but the

© 2011 The Authors, *GJI*
Geophysical Journal International © 2011 RAS

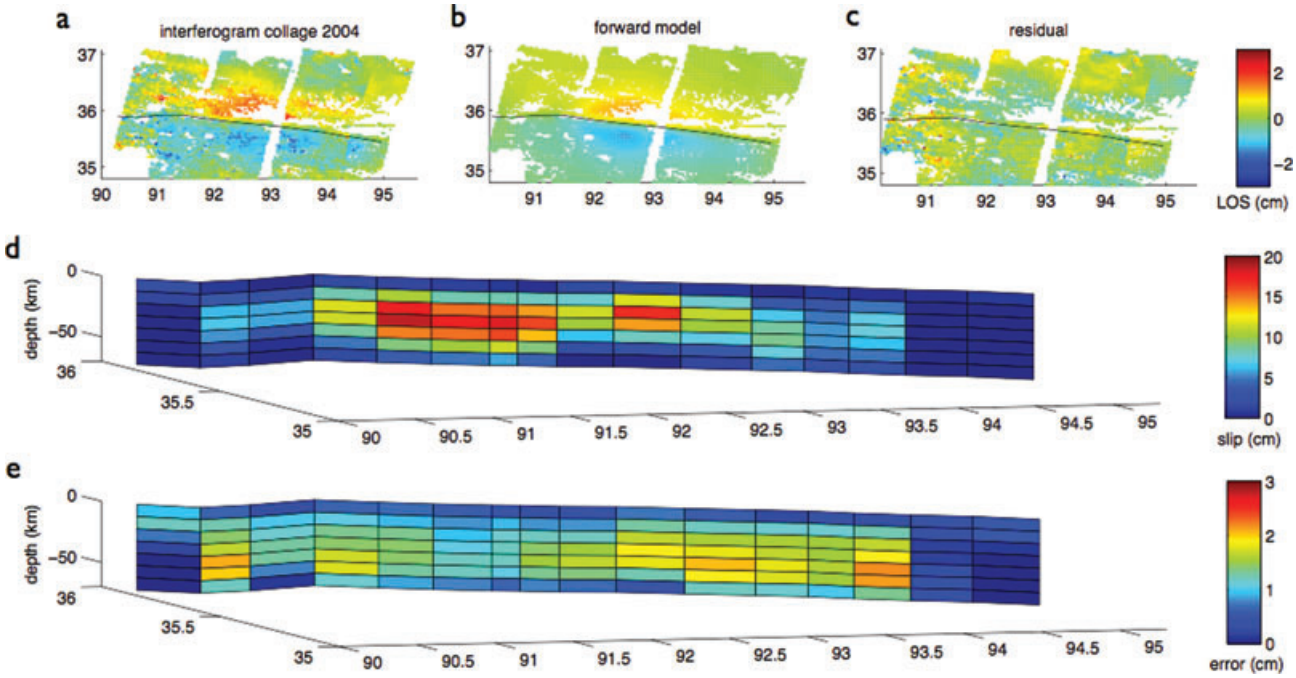

Figure 11. Results of afterslip modelling. The interferogram collage for 2004 is shown in (a), along with the synthetic equivalent (b) and residual (c). Beneath this are the estimated slip distribution (d) and its associated errors (e).

wavelength of the modelled displacement field is slightly shorter than that of the InSAR collage, which implies that the modelled afterslip distribution cannot match displacements both close to and away from the fault. In addition, horizontal displacements forward modelled at the GPS sites using the InSAR-derived afterslip distribution (and scaled to account for the earlier time window) do not give a good match to the GPS measurements (Fig. 12). This implies that either the afterslip distribution substantially changed over time, or that viscoelastic relaxation played a dominant role in relaxing the coseismic stresses (with or without afterslip). For the first possibility, the slip distribution would need to change quite markedly over time. We deem this unlikely, since other, unequivocal examples of afterslip (e.g. following the Nima-Gaize earthquake, Ryder *et al*. 2010, and also other normal faulting earthquakes on the Tibetan Plateau we have studied) show a deformation pattern that is spatially stable over time, although Bürgmann *et al*. (2002) found some modest spatial change in early afterslip inferred for the Izmit earthquake. We suggest that viscous flow is the dominant mechanism of stress relaxation, since it can explain both the early GPS and the later InSAR data set. This conclusion is supported by the results of inverting a synthetic viscoelastic data set for afterslip (Section 5), which gives a systematic misfit of horizontal displacement azimuths similar to that obtained in the real inversion.

Some afterslip is likely to have occurred as well, but probably limited to the shallow mid crust in the early post-seismic period. Recent geodetic studies of specific strike-slip earthquakes that implement stress-driven afterslip indicate that when afterslip occurs (with or without viscoelastic relaxation), it is limited to the first year or so following the earthquake (e.g. Hearn *et al*. 2009, Izmit; Barbot *et al*. 2009, Parkfield). Since our viscoelastic model does not take afterslip into account, any slip that did occur would be modelled in proxy by viscous flow, and our estimate of viscosity would therefore be a lower bound—particularly the transient viscosity, if the afterslip was concentrated during the first few months.

5.2 Lateral heterogeneity in rheological structure

Of the 13 GPS sites for which data are presented in Fig. 9, the four northernmost sites, which straddle the southern margin of the Qaidam Basin, have time-series that are over-predicted by our initial laterally homogeneous earth model. If afterslip contributes significantly to the early GPS time-series, then the asymmetry in the GPS residuals may result from a south-dipping fault and/or a change in elastic properties across the Qaidam Basin margin. Given the arguments presented above for a major contribution from viscous flow, the asymmetry may also be explained by a different rheological structure beneath the basin relative to that beneath the plateau to the south. Such a heterogeneous structure could entail a change in elastic and/or viscoelastic properties (higher rigidity/viscosity) or a change in crustal thickness, or both. There is in fact a range of independent geophysical evidence for such heterogeneity. A decrease in crustal thickness from 55 to 40 km at the boundary of the Qaidam Basin was suggested by Zhu & Helmberger (1998) as an explanation for observed teleseismic *P*-wave anomalies, and more recently Shi *et al*. (2009) and Mechie *et al*. (2011) have presented seismic evidence that supports this general inference. These authors collectively suggest that the reason for the change in crustal thickness is the strength of the Qaidam Basin relative to the weaker crust beneath the plateau, with only the latter thickening in response to the India–Eurasia collision. Other independent geophysical data suggest the possibility of a change in viscosity (and therefore strength) across either the Kunlun Fault itself or the Qaidam Basin margin. Transect 600 of the INDEPTH project runs from the Bangong–Nujiang suture zone northwards across the Qiangtang terrane in central Tibet, through the Songpan-Ganzi terrane and then across the Kunlun Shan as far north as the Qaidam Basin. Wei *et al*. (2001) and Rippe *et al*. (2010) used magnetotelluric (MT) data along this line to map high conductivity in the lower crust in the Songpan-Ganzi and Qiangtang terranes; north of the Kunlun fault, lower crustal conductivities are more in line

© 2011 The Authors, *GJI*
Geophysical Journal International © 2011 RAS

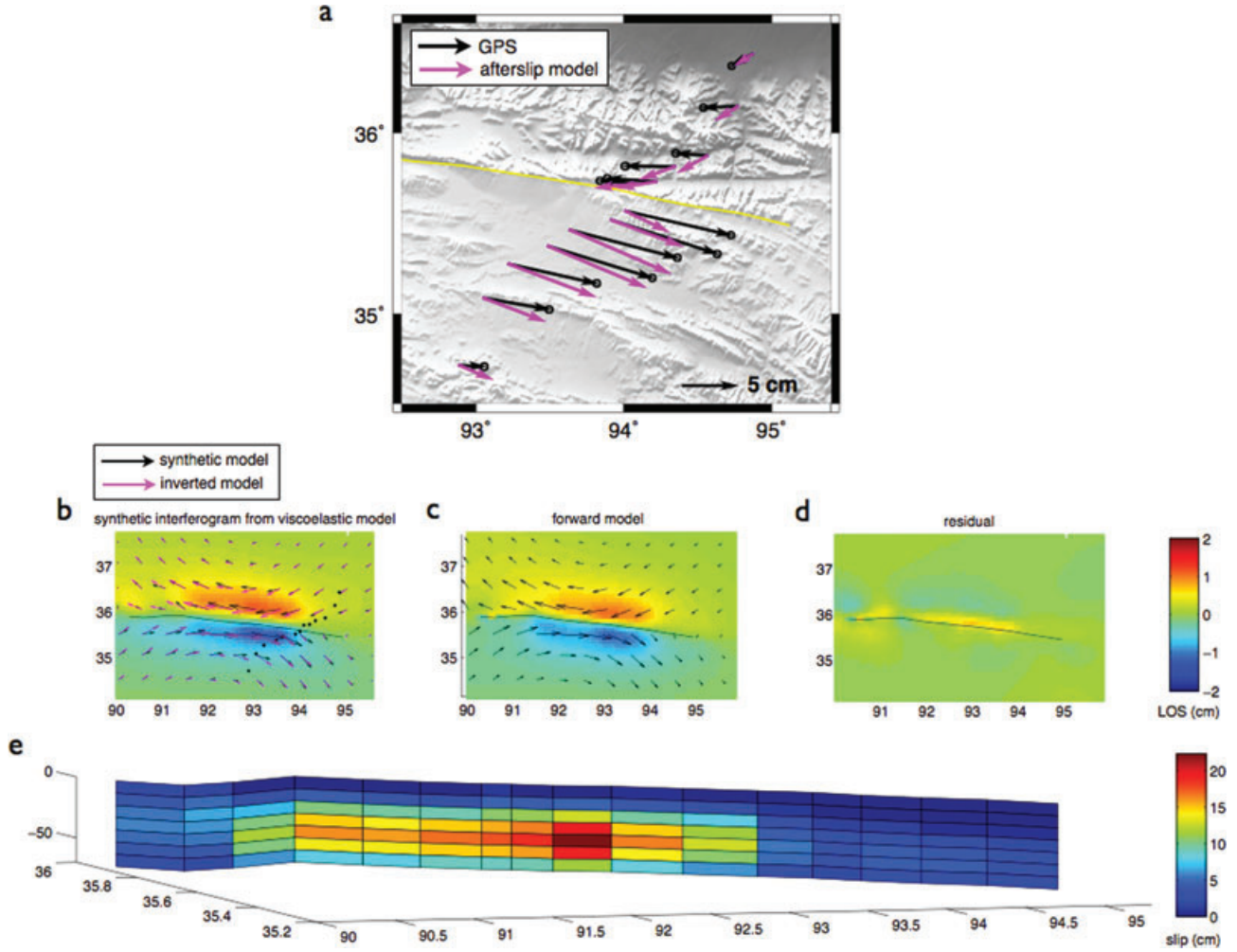

Figure 12. (a) Comparison of afterslip model with GPS displacement vectors. The model vectors are generated using the InSAR-derived slip distribution shown in Fig. 11, and scaled empirically to allow for the earlier time window of the GPS data. Below are the results of inverting a synthetic interferogram (b), which is the output of the Maxwell homogeneous crust model (same as top middle panel of Fig. 6). Black arrows show the displacements of the synthetic model and magenta arrows show the inverted displacements. Small black squares mark locations of GPS sites. Forward-modelled line of sight displacements and residuals are shown in (c) and (d), respectively, and the slip solution is shown in (e).

with those found in continental interiors. Unsworth *et al*. (2004) also mapped a decrease in conductivity across the Kunlun Fault, and in addition across the southern margin of the Qaidam Basin. Similarly, the teleseismic *P*-wave study of Owens & Zandt (1997) maps a high Poisson's ratio across the Kunlun fault up to the end of the INDEPTH line, at the southern margin of the Qaidam Basin.

To test whether a change in viscosity across the basin margin has the potential to explain the asymmetry in GPS residuals, we implement a viscoelastic model with laterally heterogeneous viscous properties, using the formulation of Pollitz (2003b). The Fortran code developed from this theoretical formulation is VISCO3D, which builds on the foundation of VISCO1D. For simplicity, a change in crustal thickness is not implemented, but we bear this in mind as an additional contributor to the asymmetry. To guide our choice of viscosity for the Qaidam Basin, we re-ran the homogeneous model with higher viscosity values, to try and improve the fit to the northern GPS stations. It was not possible to obtain a really good curve fit to the northern time-series with a homogeneous model. However, the range of viscosities (both transient and steady-state) which approximately match the magnitude of the observed northern time-series are about an order of magnitude greater $\{4\times10^{18}/4\times10^{19}/0.69\}$ than those which fit the southern time-series. Retaining the viscoelastic parameters $\{9\times10^{17}/1\times10^{19}/0.69\}$ obtained previously for the lower crust outside of the Qaidam Basin area, we apply the higher viscosities to the Qaidam Basin lower crust in our heterogeneous model. The model is constructed by specifying an elliptical area that approximately corresponds to the surface topographic expression of the Qaidam Basin (see Fig. 1), and assigning a viscosity perturbation at depth beneath this area. For both the plateau and the basin, the upper crust is again set to 16.5 km and the viscoelastic medium is set to be very thick, since the 'half space' displacements in the homogeneous model were very similar to the 65 km thick layer displacements. Other than the earth model input, the modelling procedure is very similar to that for the homogeneous case. We do not aim to produce a heterogeneous model that explains all details of the observed displacement field, but rather to illustrate the general effect of lateral heterogeneity on surface displacements along the GPS profile.

Fig. 13 shows the results of the modelling. By way of testing the heterogeneous model, the left-hand panel is a comparison of outputs from the radially symmetric model and the heterogeneous

© 2011 The Authors, *GJI*
Geophysical Journal International © 2011 RAS

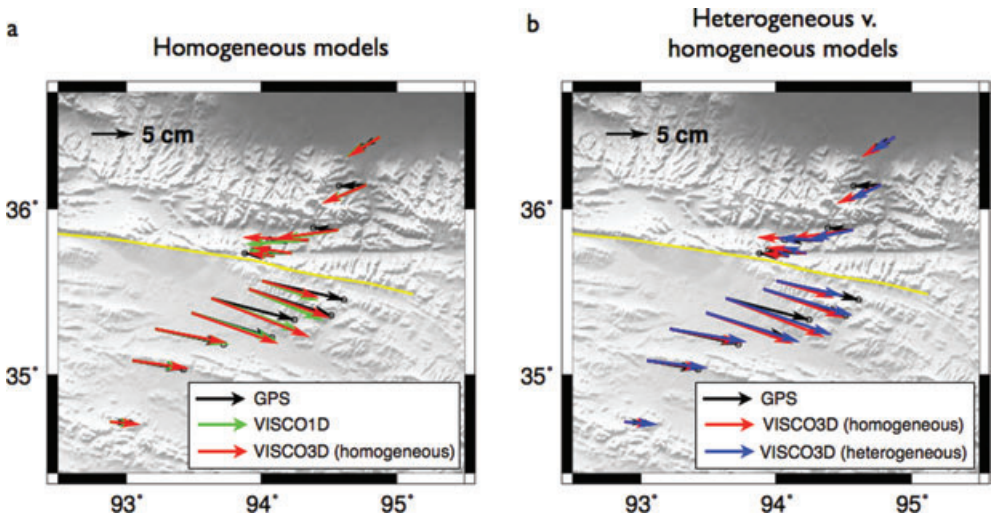

Figure 13. Results of modelling lateral heterogeneity. (a) Comparison of the homogeneous case computed with radially symmetric and lateral viscosity perturbation codes (VISCO1D and VISCO3D). (b) Comparison of the homogeneous case (red arrows) with the heterogeneous case (blue arrows) in which the Qaidam Basin viscosities are half an order of magnitude greater than under the Tibetan Plateau.

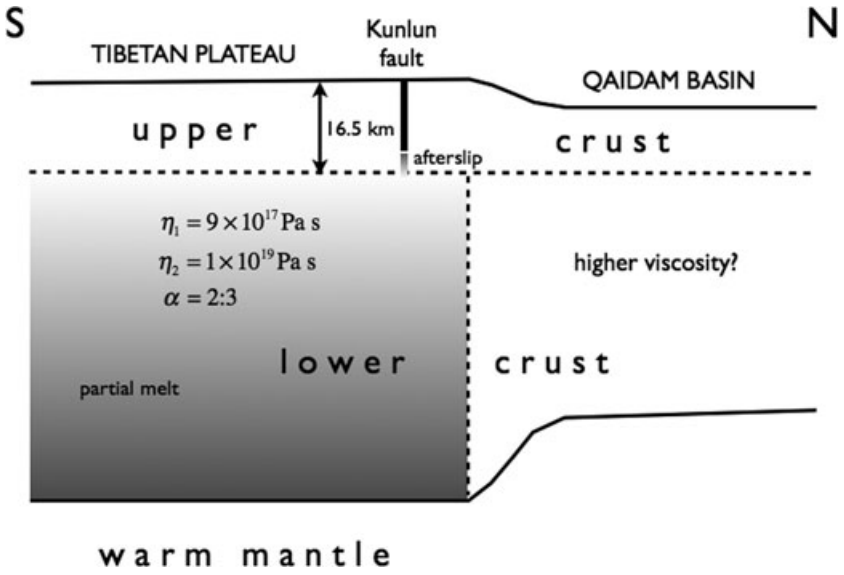

Figure 14. Schematic cross-section showing variation in rheological structure across the Kunlun fault, as inferred from this study.

model set up to simulate radial symmetry. The residuals between the two models are small and give us confidence that the heterogeneous model is a reasonable representation of lateral heterogeneity. The right-hand panel compares homogeneous and heterogeneous earth models, with viscosities $\{4\times10^{18}/4\times10^{19}\}$ under the Qaidam Basin. It can be seen that while the viscosity perturbation has very little effect on displacements to the south of the fault, it significantly reduces those on the northern side, and the effect is not limited to the four northernmost sites which the radially symmetric model over-predicts. The observed displacement at the most northerly site on the south side is under-predicted by the homogeneous model, but the heterogeneous model brings the model vector closer to the observation. This preliminary modelling gives impetus to the suggestion that the Qaidam Basin is more rigid than the Tibetan Plateau, with lower crustal viscosity values greater than the equivalent plateau values. More comprehensive modelling will be required to explore this variation in rheological structure more fully.

The schematic diagram in Fig. 14 summarises our inferred rheological structure across the Kokoxili rupture. The upper crust is labelled with a thickness of 16.5 km, which is the depth of coseismic slip estimated by Wang *et al*. (2003), but there likely exists a zone of afterslip beneath the coseismic fault rupture, which gradually merges at depth into the top of the viscoelastic layer where lower crustal flow occurs. We are not able to place constraints on the depth range or magnitude of afterslip. Viscoelastic relaxation occurs in the lower crust right down to the Moho, and possibly into the upper mantle. There may be some small increase or decrease in viscosity throughout the lower crust, but if so this would be limited to less than a factor of about three. The flow in the crust beneath the Songpan-Ganzi and Qiangtang terranes is most likely due to partial melt, for which there is independent supporting geophysical evidence. The Qaidam Basin to the north of the Kunlun Fault has a different rheological structure compared to the plateau, with higher viscosities and a thinner crust.

© 2011 The Authors, *GJI*
Geophysical Journal International © 2011 RAS

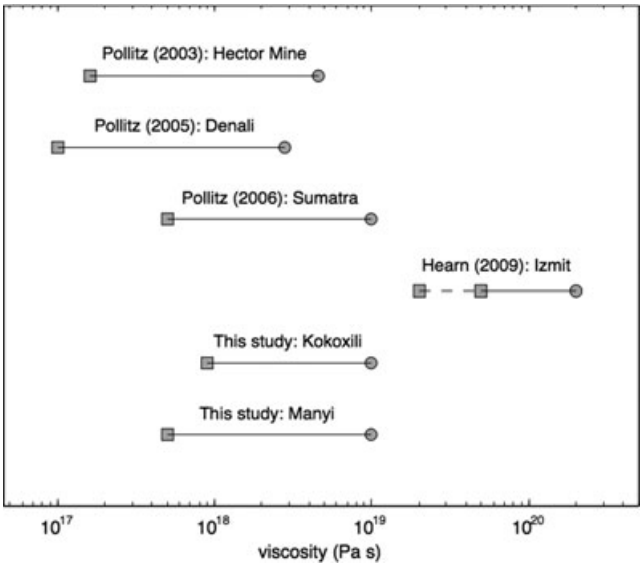

Figure 15. Values of transient viscosity (squares) and steady-state viscosity (circles) for post-seismic studies that have proposed a Burgers rheology for the lower crust or upper mantle.

5.3 Lower crustal rheology

In this study, we infer that viscous flow in the lower crust (and possibly the upper mantle) is responsible for at least some of the observed post-seismic surface deformation following the 2001 Kokoxili earthquake. A relatively simple model of flow in a homogeneous crust with a Burgers rheology is sufficient to explain the first-order spatial and temporal characteristics of the geodetic data sets. Although several other investigations of post-seismic stress relaxation have inferred a biviscous upper mantle (Pollitz *et al*. 2003, 2006; Pollitz 2005), this study is the first to propose a Burgers-type behaviour for the lower crust. For all Burgers rheology case studies, the transient and steady-state viscosities vary by about 1–1.5 orders of magnitude, as illustrated in Fig. 15. This is of interest in light of the conclusion by Chopra (1997) that natural dunites deformed in the laboratory can be effectively modelled in terms of a Burgers rheology, and that the ratio η_1/η_2 for these rocks is relatively insensitive to temperature and stress. For some earthquakes for which a Burgers rheology has been proposed, for example the 1999 Hector Mine event (Pollitz 2003a) and the 2002 Denali event (Pollitz 2005), other workers have shown that a power-law rheology also provides a reasonable fit to surface geodetic data (Freed & Bürgmann 2004; Freed *et al*. 2006). For a Burgers body, viscosity values of both the Maxwell and Kelvin elements are constant. However, during post-loading stress relaxation, dominance passes from the Kelvin to the Maxwell element over time. Since at any one time both elements contribute to the overall deformation, this means that effective viscosity changes over time. It can thus be seen that a Burgers rheology can in fact approximate a power-law rheology, whose effective viscosity is stress-dependent and therefore does actually change during the post-seismic phase as stresses are relaxed. Distinguishing between these two functionalities is therefore not straightforward.

Although it has been known since the INDEPTH seismic/MT studies starting in the mid-1990s that the lower crust in northern Tibet is highly conductive, only recently have the results of these studies been tied into the results of laboratory experiments to make quantitative estimates of crustal viscosity, assuming that high conductivities are due to the presence of partial melt in the lower crust. Rippe & Unsworth (2010) inferred flow rates and viscosity values for a compilation of MT measurements of conductance (integrated conductivity over depth), drawing on various published laboratory measurements of partial melts. For the Qiangtang terrane, Rippe & Unsworth (2010) inferred an effective viscosity range of 2.5×10^{18}–3×10^{20} Pa s for granites, depending on whether the conducting layer is assumed to have constant thickness or constant bulk resistivity. For aplites, the effective viscosity range is 4.5×10^{16}–8×10^{19} Pa s. As Rippe & Unsworth (2010) point out, there are many assumptions involved in their estimation of viscosity. However, it is worth noting that the wide range of viscosities constrained by their study span the values of steady-state viscosity obtained in this study.

Fig. 16 shows a 50-yr projection of east–west post-seismic displacements at GPS site BDGD, which is located about 5 km south of the fault. Cumulative displacements in 2020 are predicted to have reached 42 cm; for 2050, the prediction is 60 cm. Continued geodetic measurements in this region are therefore to be encouraged, to test whether a Burgers description of the lower crust is viable over decadal timescales.

5.4 The 1997 Manyi earthquake

Ryder *et al*. (2007) found that both viscous flow in the lower crust and deep afterslip can explain the observed post-seismic transient following the 1997 Manyi earthquake. From the viscoelastic relaxation modelling, it was found that to match the observed time dependence of the surface displacements, the lower crust was required to have two time constants; in this case a standard linear solid

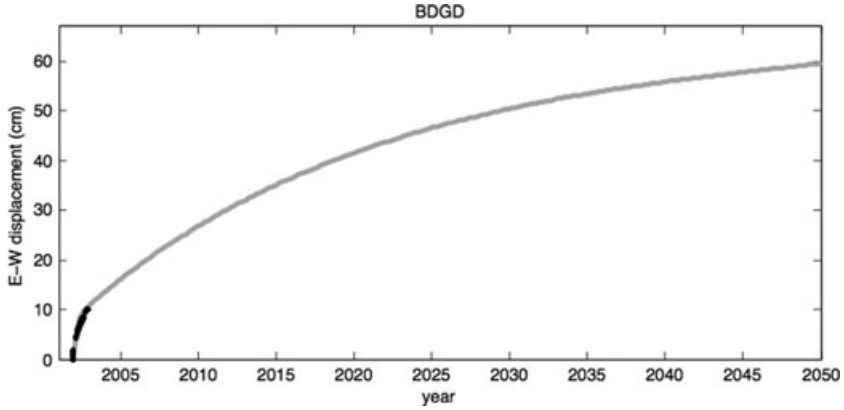

Figure 16. Projection of east–west displacement at GPS site BDGD up to the year 2050, according to our optimal Burgers rheology model.

© 2011 The Authors, *GJI*
Geophysical Journal International © 2011 RAS

was used, with an optimal viscosity of 4×10^{18} Pa s and a relaxation in shear modulus of one third. The relaxation in shear modulus is the same as the Burgers body equivalent obtained in the present Kokoxili study, while the best-fit viscosity, which provides a reasonable fit to the Manyi data irrespective of time period, is in between the values of transient and steady-state viscosities estimated for the Kokoxili region. Bell *et al.* (2010) extended the InSAR data set of Ryder *et al.* (2007) beyond a decade from the Manyi earthquake and found that displacement rates of 1 cm yr^{-1} occurred in the twelfth post-seismic year. Since it is unlikely that afterslip would continue for such a long period of time, this deformation is indicative of viscoelastic relaxation in the lower crust.

Here, we model the lower crust in the Manyi region using a Burgers rheology instead of a standard linear solid rheology, to test whether the same parameters obtained from the Kokoxili study are applicable 250 km along strike to the west. For the four Manyi post-seismic interferograms listed in Table 4, some of which are shown in fig. 4 of Ryder *et al*. (2007), we model surface line-of-sight displacements along cross-fault profiles in an analogous way to the Kokoxili modelling. The interferograms are chosen from Tracks 305 and 33, which between them cover most of the surface deformation field (see fig. 4 of Ryder *et al*. 2007). To test whether the Burgers model successfully reproduces the time dependence of the transient, the interferograms have a range of temporal coverage over the first four post-seismic years. We start by simply taking the optimal

Table 4. Post-seismic interferograms for the Manyi earthquake. Profiles across the fault for each interferogram are shown in Fig. 17.

Track	desc/asc	Start	End	Years	B_{perp} (m)
305	desc	19971202	19980804	0.67	69
305	desc	19980210	20001226	1.92	32
33	desc	19971218	19991223	2.01	26
33	desc	19991223	20010913	1.72	49

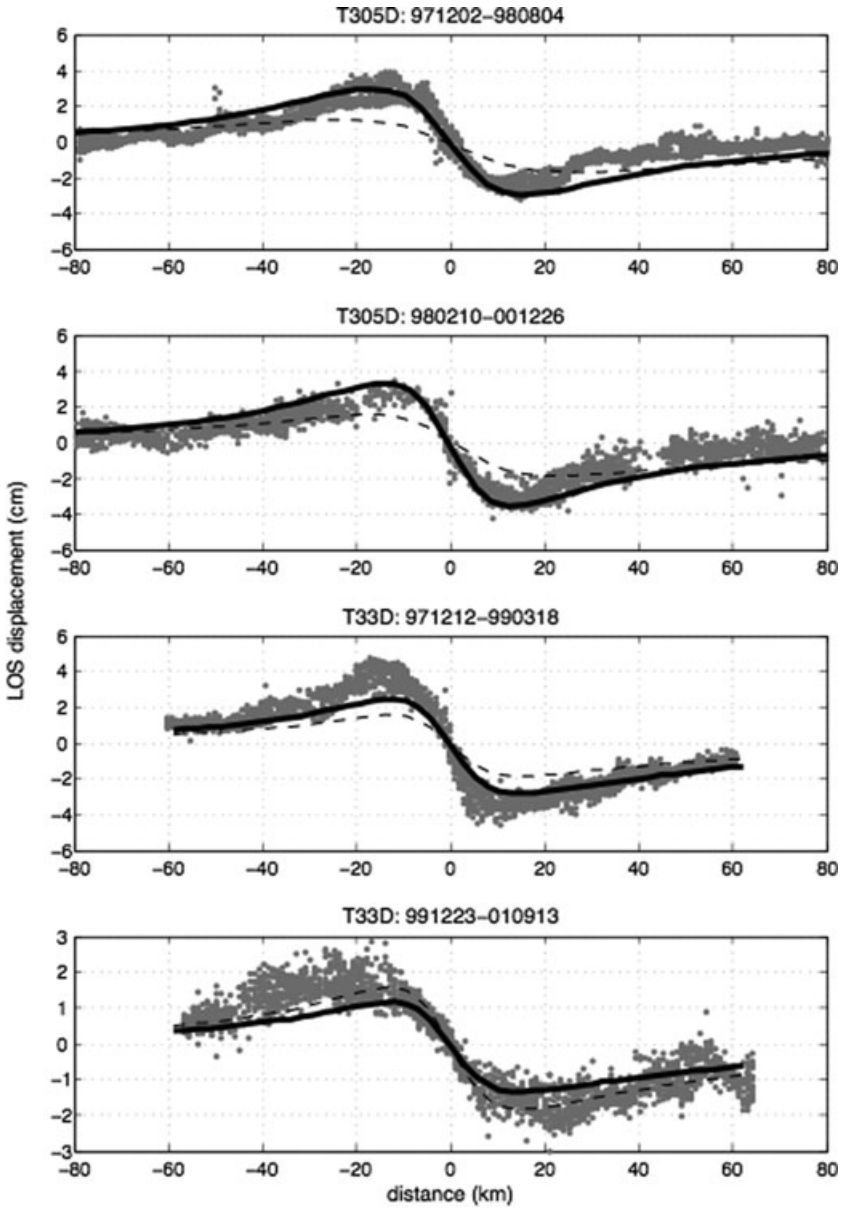

Figure 17. InSAR line of sight displacements (grey dots) along profiles across the Manyi fault that ruptured in 1997, with predictions of the optimal Burgers model (solid lines), and also the model inferred for the Kokoxili area (dashed lines).

© 2011 The Authors, *GJI*
Geophysical Journal International © 2011 RAS

Burgers parameters from the Kokoxili analysis and running models for the time periods covered by the Manyi interferograms. The upper layer thickness is set to be 16 km and the viscoelastic medium is designated as a half-space.

Fig. 17 shows profiles across the interferograms, and the thin dashed lines show the predictions of the Kokoxili-type rheological model. InSAR displacements are shown for pixels within 10 km of the model profile line. The model displacements are the correct order of magnitude, but under-predict the observed displacements for three out of the four profiles, and also make the wavelength of the Track 305 profiles too broad (thin dashed lines in Fig. 17). A significantly better fit is achieved if the transient viscosity is modified to $\eta_1 = 5 \times 10^{17}$ Pa s (thicker solid black lines in Fig. 17), that is, if the transient viscosity in the Manyi area is about 30 per cent lower than in the Kokoxili area. The shear modulus ratio α is the same for both areas. There is no clear discrepancy between the goodness of fit on the southern and northern sides of the fault, suggesting that lateral heterogeneity in viscous properties is not as pronounced here as it is further east across the plateau-bounding Kunlun fault. This is consistent with there being no basin adjacent to the Manyi area. The suggested difference in viscosity along strike is small compared to the several orders of magnitude variation in viscosity that has been proposed by various workers for the Tibetan lower crust (Clark & Royden 2000; Shen *et al*. 2001; Hilley *et al*. 2009). A distance of about 250 km separates the Manyi and Kokoxili areas, and so it is perhaps not surprising that there is some small degree of heterogeneity. Cenozoic volcanic rocks mapped in the eastern Songpan-Ganzi and Qiangtang terranes crop out west of 92° (e.g. Ding *et al*. 2003), that is, west of most of the Kokoxili deformation, and the Manyi area in particular has many examples of potassic volcanic rocks around Ulugh Muztagh. If the presence of these volcanics is indicative of the extent of partial melt in the lower crust, and partial melt facilitates the initial creep response to the coseismic stress changes through its presence at grain boundaries, this might explain the lower transient viscosity in the Manyi area.

6 CONCLUSIONS

In this study, we have analysed geodetic data sets to place robust constraints on the rheological structure and properties of the crust beneath the northeastern Tibetan plateau. A combination of early (one year) GPS data and later (years two to five) InSAR data following the 2001 Kokoxili earthquake allows us to infer stress relaxation by flow in a warm mid to lower crust beneath the plateau with a biviscous rheology (transient viscosity 9×10^{17} Pa s and steady-state viscosity 1×10^{19} Pa s). The mechanical properties of the crust vary from north to south across the fault, with thinner crust/higher viscosities beneath the Qaidam Basin relative to the plateau. Afterslip throughout the thick Tibetan lower crust can give a reasonable match to the InSAR observations in the third post-seismic year, but (i) the modelled deformation lobes are slightly less broad than those observed, and (ii) using the afterslip distribution to model the early GPS displacement vectors gives a systematic azimuthal mismatch either side of the fault. We infer that afterslip cannot have been the only mechanism of stress relaxation, although some degree of (early) afterslip is likely to have occurred, in which case our estimated viscosity values would represent lower bounds. From reanalysis of the post-seismic InSAR data set for the 1997 Manyi earthquake using a Burgers rheology, some modest rheological heterogeneity is inferred along strike, with a slightly lower transient viscosity (5×10^{17} Pa s) beneath the Manyi region. Model predictions of surface deformation near the Kokoxili rupture in the future suggest that up to 60 cm of east–west displacement may occur by the year 2050, so further observation of stress relaxation in this area is warranted.

ACKNOWLEDGMENTS

This work is supported by NSF grant EAR 073829. All Envisat data were obtained from the European Space Agency.

REFERENCES

Avouac, J.P. & Tapponnier, P., 1993. Kinematic model of active deformation in central Asia, *Geophys. Res. Lett.,* **20,** 895–898.

Bai, D. *et al*., 2010. Crustal deformation of the eastern Tibetan plateau revealed by magnetotelluric imaging, *Nat. Geosci.,* **3,** 358–362.

Barbot, S., Fialko, Y. & Bock, Y., 2009. Postseismic deformation due to the Mw 6.0 2004 Parkfield earthquake: stress-driven creep on a fault, with spatially variable rate-and-state friction parameters, *J. geophys. Res.,* **114,** B07405, doi:10.1029/2008JB005748.

Bell, M.A., Parsons, B.E. & Ryder, I.M., 2010. Postseismic motion of the 1997 Manyi Earthquake continuing to the present, *AGU Fall Meeting 2010*, abstract #T43B-2188.

Biggs, J., Bürgmann, R., Freymueller, J., Lu, Z., Parsons, B., Ryder, I., Schmalzle, G. & Wright, T., 2009. The postseismic response to the 2002 *M* 7.9 Denali Fault earthquake: constraints from InSAR 2003–2005, *Geophys. J. Int.,* **176,** 353–367, doi:10.1111/j.1365-246X.2008.03932.x.

Bürgmann, R. & Dresen, G., 2008. Rheology of the lower crust and upper mantle: Evidence from rock mechanics, geodesy and field observations, *Ann. Rev. Earth Plan. Sci.,* **36,** 531–567, doi:10.1146/annurev.earth.36.031207.124326.

Bürgmann, R., Ergintav, S., Segall, P., Hearn, E. H., McClusky, S., Reilinger, R.E., Woith, H. & Zschau, J., 2002. Time-space variable afterslip on and deep below the Izmit earthquake rupture, *Bull. seism. Soc. Am.,* **92,** 126–137.

Chopra, P.N., 1997. High-temperature transient creep in olivine rocks, *Tectonophysics,* **279,** 93–111.

Clark, M. K. & Royden, L. H., 2000. Topographic ooze: building the eastern margin of Tibet by lower crustal flow, *Geology,* **28,** 703–706.

Ding, L., Kapp, P., Zhong, D. & Deng, W., 2003. Cenozoic volcanism in Tibet: Evidence for a transition from oceanic to continental subduction, *J. Petrol.,* **44,** 1833–1865.

England, P. & Molnar, P., 1997. Active deformation of Asia, from kinematics to dynamics, *Science,* **278,** 647–650.

Fan, G.-W. & Lay, T., 2003. Strong Lg attenuation in the Tibetan Plateau, *Bull. seism. Soc. Am.,* **93**(5), 2264–2272, doi:10.1785/0120030052.

Freed, A. M. & Bürgmann, R., 2004. Evidence of power-law flow in the Mojave desert mantle, *Nature,* **430,** 548–551.

Freed, A. M., Bürgmann, R., Calais, E. & Freymueller, J., 2006. Stress-dependent power-law flow in the upper mantle following the 2002 Denali, Alaska, earthquake, *Earth planet. Sci. Lett.,* **252,** 481–489.

Hacker, B.R., Gnos, E., Ratschbacher, L., Grove, M., McWilliams, M., Sobolev, S.V., Wan, J. & Wu, Z. 2000. Hot and dry deep crustal xenoliths from Tibet, *Science,* **287,** 2463–2466.

Haibing, L., Van der Woerd, J., Tapponnier, P., Klinger, Y., Xuexiang, Q., Jingsui, Y. & Yintang, Z., 2005. Slip rate on the Kunlun fault at Hongshui Gou, and recurrence time of great events comparable to the 14/11/2001, Mw∼7.9 Kokoxili earthquake, *Earth planet. Sci. Lett.,* **237,** 285–299.

Hearn, E. H., Bürgmann, R. & Reilinger, R., 2002. Dynamics of Izmit earthquake postseismic deformation and loading of the Duzce earthquake hypocenter, *Bull. seism. Soc. Am.,* **92,** 172–193.

Hearn, E. H., McClusky, S., Ergintav, S. & Reilinger, R. E., 2009. Izmit earthquake postseismic deformation and dynamics of the North Anatolian Fault Zone, *J. geophys. Res.,* **114,** B08405, doi:10.1029/2008JB006026.

Hilley, G. E. Johnson, K.M., Wang, M., Shen, Z-K. & Bürgmann, R., 2009. Earthquake-cycle deformation and fault slip rates in northern Tibet, *Geology,* **37,** 31–34.

© 2011 The Authors, *GJI*
Geophysical Journal International © 2011 RAS

Houseman, G. & England, P., 1993. Crustal thickening versus lateral expulsion in the Indian-Asian continental collision, *J. geophys. Res.,* **98**(B7), 12 233–12 249.

Jacobs, A., Sandwell, D., Fialko, Y. & Sichoix, L., 2002. The 1999 (Mw 7. 1) Hector Mine, California, earthquake, Near-field postseismic deformation from ERS interferometry, *Bull. seism. Soc. Am.,* **92,** 1433–1442.

Johnson, K.M., Bürgmann, R. & Freymueller, J.T., 2006. Coupled afterslip and viscoelastic flow following the 2002 Denali Fault, Alaska Earthquake, *Geophys. J. Int.,* **176,** 670–682, doi:10.1111/j.1365-1246X.2008.04029.

Klemperer, S.L., 2006. Crustal flow in Tibet: geophysical evidence for the physical state of Tibetan lithosphere, and inferred patterns of active flow, *Geol. Soc. Lond. Spec. Publ.,* **268,** 39–70, doi:10.1144/GSL.SP.2006.268.01.03.

Lasserre, C., Peltzer, F., Crampé, F., Klinger, Y., Van der Woerd, J. & Tapponnier, P., 2005. Coseismic deformation of the 2001 M-w = 7.8 Kokoxili earthquake in Tibet, measured by synthetic aperture radar interferometry, *J. geophys. Res.,* **110**(B12), doi:10.1029/2004JB003500.

McNamara, D. E., Walter, W.R., Owens, T.J. & Ammon, C.J., 1997. Upper mantle velocity structure beneath the Tibetan Plateau from Pn travel time tomography, *J. geophys. Res.,* **102**(B1), 493–505.

Meade, B. J., 2007. Present-day kinematics at the India-Asia collision zone, *Geology,* **35,** 81–84.

Mechie, J., Kind, R. & Saul, J., 2011. The seismological structure of the Tibetan Plateau crust and mantle down to 700 km depth, *Geol. Soc. Lond. Spec. Publ.,* **353,** 109–125.

Ni, J. & Barazangi, M. 1983. High-frequency seismic wave propagation beneath the Indian Shield, Himalayan Arc, Tibetan plateau and surrounding regions; high uppermost mantle velocities and efficient Sn propagation beneath Tibet, *Geophys. J. R. astr. Soc.,* **72,** 665–689.

Owens, T. J. & Zandt, G., 1997. Implications of crustal property variations for models of Tibetan plateau evolution, *Nature,* **387,** 37–43.

Pollitz, F. F., 1992. Postseismic relaxation theory on the spherical earth, *Bull. seism. Soc. Am.,* **82,** 422–453.

Pollitz, F. F., 2003a. Transient rheology of the uppermost mantle beneath the Mojave Desert, California, *Earth planet. Sci. Lett.,* **215,** 89–104.

Pollitz, F.F., 2003b. Post-seismic relaxation theory on a laterally heterogeneous viscoelastic model, *Geophys. J. Int.,* **155,** 57–78.

Pollitz, F. F., 2005. Transient rheology of the upper mantle beneath central Alaska inferred from the crustal velocity field following the 2002 Denali earthquake, *J. geophys. Res.,* **110**(B8), doi:10.1029/2005JB003672.

Pollitz, F. F., Bürgmann, R. & Banerjee, P., 2006. Post-seismic relaxation following the great 2004 Sumatra-Andaman earthquake on a compressible self-gravitating Earth, *Geophys. J. Int.,* **167,** 397–420.

Rapine R., Tilmann, F., West, M., Ni, J. & Rodgers, A., 2003. Crustal structure of northern and southern Tibet from surface wave dispersion analysis, *J. geophys. Res.,* **108,** 2120, doi:10.1029/2001JB000445.

Ren, J. & Wang, M., 2005. GPS measured crustal deformation of the Ms8.1 Kunlun earthquake on November 14th 2001 in Qinghai-Xizang plateau, *Quat. Sci.,* **25,** 34–44.

Rippe, D. & Unsworth, M., 2010. Quantifying crustal flow in Tibet with magnetotelluric data, *Phys. Earth planet. Inter.,* **179,** 107–121.

Robinson, D. P., Brough, C. & Das, S., 2006. The Mw 7.8, 2001 Kunlunshan earthquake, Extreme rupture speed variability and effect of fault geometry, *J. geophys. Res.,* **111**(B8), B08303, doi:10.1029/2005JB004137.

Rodgers, A. J. & Schwartz, S. Y., 1998. Lithospheric structure of the Qiangtang Terrane, northern Tibetan Plateau, from complete regional waveform modeling: Evidence for partial melt, *J. geophys. Res.,* **103**(B4), 7137–7152.

Rosen, P. A., Hensley, S. & Peltzer, G., 2004. Updated repeat orbit interferometry package released, *EOS, Trans. Am. geophys. Un.,* **85**(5), 35.

Rosenberg, C.L. & Handy, M.R., 2005. Experimental deformation of partially melted granite revisited; implications for the continental crust, *J. Metamorph. Geol.* **23,** 19–28.

Royden, L. H., Burchfiel, B.C., King, R.W., Wang, E., Chen, Z., Shen, F. & Liu, Y., 1997. Surface deformation and lower crustal flow in Eastern Tibet, *Science,* **276**(5313), 788–790.

Ryder, I., Parsons, B., Wright, T.J. & Funning, G., 2007. Post-seismic motion following the 1997 Manyi, Tibet earthquake, InSAR observations and modelling, *Geophys. J. Int.,* **169,** 1009–1027.

Ryder, I., Bürgmann, R. & Sun, J., 2010. Tandem afterslip on connected fault planes following the 2008 Nima-Gaize, Tibet earthquake, *J. geophys. Res.,* **115,** B03404, doi:10.1029/2009JB006423.

Savage, J. C., 1990. Equivalent strike-slip earthquake cycles in half-space and lithosphere-asthenosphere Earth models, *J. geophys. Res.,* **95**(B4), 4873–4879.

Savage, J. C. & Burford, R. O., 1973. Geodetic determination of relative plate motion in Central California, *J. geophys. Res.,* **78,** 832–845.

Shapiro, N.M., Ritzwoller, M.H., Molnar, P. & Levin, V., 2004. Thinning and flow of Tibetan crust constrained by seismic anisotropy, *Science,* **305,** 233–236.

Shen, Z.-K., Zeng, Y., Wang, M., Wang, Q., Wang, Q.-L., Wan, Y., Gan, W. & Zhang, Z., 2003. Postseismic deformation modeling of the 2001 Kokoxili earthquake, western China, *Abstracts, EGS-AGU-EUG Joint Assembly*.

Shen, F., Royden, L.H. & Burchfiel, B.C., 2001. Large-scale crustal deformation of the Tibetan Plateau, *J. geophys. Res.,* **106**(B4), 6793–6816.

Shi, D., Shen, Y., Zhao, W. & Li, A., 2009. Seismic evidence for a Moho offset and south-directed thrust at the easternmost Qaidam-Kunlun boundary in the Northeast Tibetan plateau, *Earth planet. Sci. Lett.,* **288,** 329–334.

Sun, J.B., Shen, Z. & Bürgmann, R., 2008. Synthetic normal faulting of the 9 January 2008 Nima, Tibet earthquake from conventional and along-track SAR interferometry, *Geophys. Res. Lett.,* **35,** doi:10.1029/2008GL035691.

Unsworth, M., 2010. Magnetotelluric studies of active continent–continent collisions, *Surv. Geophys.,* **1,** 137–161, doi:10.1007/s10712-009-9086-y.

Unsworth, M. *et al*., 2004, Crustal and upper mantle structure of northern Tibet imaged with magnetotelluric data, *J. geophys. Res.,* **109,** B02403, doi:10.1029/2002JB002305.

Van der Woerd, J. *et al.*, 1998. Holocene left-slip rate determined by cosmogenic surface dating on the Xidatan segment of the Kunlun fault, Qinghai, China, *Geology,* **26,** 695–698.

Vergne, J., Wittlinger, G., Qiang H., Tapponnier, P., Poupinet, G., Jiang M., Herquel, G. & Paul, A. 2002. Seismic evidence for stepwise thickening of the crust across the NE Tibetan Plateau, *Earth planet. Sci. Lett.,* **203,** 25–33.

Wang, M., Wan, Y., Shen, Z., Chen, J., Zhang, Z., Gan, W. & Wang, Q., 2003. Slip distribution of the 2001 M_w Kokoxili earthquake, western China, *AGS-AGU-AUG Joint Assembly,* Nice, 2003, abstract #5549.

Wei, W. B. *et al*., 2001. Detection of widespread fluids in the Tibetan crust by magnetotelluric studies, *Science,* **292,** 716–718.

Woerd, J. V.D. *et al*., 2002. Uniform postglacial slip-rate along the central 600 km of the Kunlun Fault, Tibet, from ^{26}Al, ^{10}Be, and ^{14}C dating of riser offsets, and climatic origin of the regional morphology, *Geophys. J. Int.,* **148,** 356–388.

Wright, T. J., Parsons, B., England, P.C. & Fielding, E.J., 2004. InSAR observations of low slip rates on the major faults of western Tibet. *Science,* **305,** 236–239.

Xiong, X., Shan, B., Zheng, Y. & Wang, R., 2010. Stress transfer and its implication for earthquake hazard on the Kunlun Fault, Tibet, *Tectonophysics,* **482,** 216–225.

Zhang, P.-Z. *et al*., 2004. Continuous deformation of the Tibetan Plateau from global positioning system data, *Geology,* **32,** 809–812.

Zhu, L. P. & Helmberger, D. V., 1998. Moho offset across the northern margin of the Tibetan Plateau, *Science,* **281,** 1170–1172.

© 2011 The Authors, *GJI*
Geophysical Journal International © 2011 RAS